Year-Round High-Resolution Sea Ice Freeboard Retrieval Using ICESat-2 ATL03 Photon Data

Wenxuan Liu[1,2,3], Ruibo Lei[1,2,3], Taoyong Jin[4], Heyang Sun[4], Michel Tsamados[5], Isolde A. Glissenaar[6], Jack Christopher Landy[6], Yi Zhou[1,7]

[1]MNR Key Laboratory of Polar Science, Polar Research Institute of China, Shanghai, China
[2]National Arctic and Antarctic Data Center, Polar Research Institute of China, Shanghai, China
[3]Arctic Yellow River Earth System National Observation and Research Station
[4]MOE Key Laboratory of Geospace Environment and Geodesy, School of Geodesy and Geomatics, Wuhan University, Wuhan, China
[5]Centre for Polar Observation and Modelling, Department of Earth Sciences, University College London, London, United Kingdom
[6]Department of Physics and Technology, UiT The Arctic University of Norway, Tromsø, Norway
[7]School of Oceanography and the Key Laboratory of Polar Ecosystem and Climate Change, Ministry of Education, Shanghai Jiao Tong University, Shanghai, China

Correspondence to: Ruibo Lei (leiruibo@pric.org.cn)

Abstract. Arctic sea ice freeboard is critical for estimating ice thickness and characterizing surface morphology, yet it remains poorly constrained, especially during the melt season due to limitations in conventional altimetry products. The ICESat-2 ATL07 product retrieves surface heights using variable along-track segment lengths (10–200 m) and identifies floes and leads using fixed thresholds based on photon rate, background rate, and width of the photon distribution to support freeboard estimation. This strategy can smooth ice-ridge-related features and reduce reliability over sea ice surfaces with complex spatial variations or melt-affected conditions. To address these challenges, we present a year-round, high-resolution (5 m) freeboard retrieval method (HRFM) based directly on ICESat-2 ATL03 photon data. A two-stage denoising strategy is implemented to robustly extract signal photons, while a machine-learning classifier, trained using 25 coincident Sentinel-2/ICESat-2 scenes, discriminates between sea ice, thin ice, and leads under both winter and summer surface conditions. Identified lead segments are used to construct local sea-surface references for freeboard estimation. Validation against Airborne Topographic Mapper (ATM) data shows that HRFM reduces the surface-height root-mean-square error (*RMSE*) for strong beams from 0.12 m (ATL07) to 0.08 m (by 33%). HRFM better preserves ridge-related heights that are smoothed in ATL07. The classifier attains a precision of 0.96 and a recall of 0.95 for lead detection, supporting reliable freeboard estimation. Weak-beam retrievals also show encouraging validation performance under the same evaluation framework. During the one-year demonstration period, the spatial patterns of retrieved freeboard are broadly consistent with the ICESat-2 ATL20 product, while monthly mean differences between the two products reach up to 0.04 m. By improving topographic fidelity and lead detection, HRFM provides a framework for high-resolution freeboard retrieval under both winter and summer surface conditions.

删除了: [3]
删除了: [3]
删除了: [4]
删除了: [5]
删除了: [1]
删除了: [6]
设置了格式: 上标
删除了: [3]MOE
删除了: [4]Centre
删除了: [5]Department
删除了: [6]School

删除了: s
删除了: The ICESat-2 ATL07 product retrieves surface heights at variable along-track segment lengths (10 ‑ 200 m) and identifies floes and leads using fixed thresholds (photon rate, background rate and the width of height distribution) to support freeboard estimation,
删除了: which
删除了: s
删除了: small-scale
删除了: s
删除了:
删除了: affected by melting
删除了: on
删除了: Sentinel-2 images
删除了: across seasons
删除了: Identified lead segments provide local sea surface references from which freeboard is estimated.
删除了: ,
删除了: while weak-beam retrievals achieve comparable accuracy.
删除了: that are underestimated by ATL07.
删除了: cation
删除了: After applying the method at a pan-Arctic scale
删除了: but with seasonal mean differences reaching up to 0.04 m
删除了: By improving both topographic fidelity and lead detection, HRFM mitigates common limitations of ICESat-2 sea ice products and enables high-resolution freeboard estimates across seasons.

1 Introduction

Arctic sea ice plays a pivotal role in regulating exchanges of heat (Aylmer et al., 2024), momentum (Muilwijk et al., 2024), and water vapor (Ridley et al., 2023) between the atmosphere and oceans, with impacts spanning local processes to the global climate system (Sun et al., 2018). Changes in sea ice thickness are widely recognized as a key indicator of climate change (Stroeve and Notz, 2018), influencing the surface energy balance (Von Schuckmann et al., 2023; Zhou et al., 2025), ocean–atmosphere interactions (McPhee, 2008; Timmermans and Marshall, 2020), high-latitude biodiversity (Macias-Fauria and Post, 2018; Pratte et al., 2019), and Arctic shipping operations (Shu et al., 2024). Sea ice freeboard, defined as the height of the ice surface above the local sea level, is a fundamental parameter for estimating ice thickness from satellite altimeters (Kacimi and Kwok, 2024), for characterizing surface roughness relevant to stress and momentum transfer (Krumpen et al., 2025; Mchedlishvili et al., 2023), as well as for parameterizing mechanical interactions between sea ice and ships or platforms (Lund et al., 2025). Despite its importance for quantifying ice mass balance and improving sea ice forecasts (Liu et al., 2025; Song et al., 2024), obtaining sustained, high-resolution, and year-round spaceborne observations of freeboard remain challenging. This difficulty is largely related to the limitations of current altimetric retrieval frameworks in robustly retrieving both ice surface heights and local sea levels, particularly across the pan-Arctic and under seasonally varying surface conditions.

Satellite altimeters retrieve freeboard as the difference between the measured ice surface height and the local sea level inferred from leads or open water (Laxon et al., 2013; Quartly et al., 2019). Consequently, the accuracy of freeboard estimation depends mainly on two key processes: precise surface height retrieval and robust surface type classification. Earlier lidar and radar missions, such as ICESat (Ice, Cloud, and land Elevation Satellite; Schutz et al., 2005) and CryoSat-2 (Wingham et al., 2006), provided valuable insights into sea ice freeboard and thickness (Kurtz and Markus, 2012; Landy et al., 2022). Notably, recent advances in lead detection using machine learning applied to CryoSat-2 data have enabled the first year-round radar freeboard products (Dawson et al., 2022; Landy et al., 2022), underscoring the importance of improved surface-type classification for extending the year-round applicability of altimetric freeboard retrievals. Launched in 2018, ICESat-2 (IS-2) represents a major advance in ice surface altimetry. Equipped with the Advanced Topographic Laser Altimeter System (ATLAS), a photon-counting lidar, IS-2 reduced the along-track footprint from approximately 170 m (ICESat) to 11 m (Magruder et al., 2020), improving elevation precision and the capacity to resolve small-scale surface roughness (Markus et al., 2017; Ricker et al., 2023) and thereby supporting more accurate surface-type classification. ATLAS acquires data via six beams organized into three beam pairs, each consisting of one strong beam and one weak beam with a 4:1 transmit-energy ratio. While this configuration enhances spatial coverage, the lower signal-to-noise ratio of the weak beam poses challenges for data processing. The ATL03 product supplies geolocated photon clouds and constitutes the raw observational source from which all higher-level IS-2 products are derived (Neumann et al., 2019). Operating at a wavelength of 532 nm, IS-2 measurements primarily reflect from the air-snow interface; Thus, the derived freeboard is typically defined as the total snow + ice freeboard (Kacimi and Kwok, 2022; Magruder et al., 2025).

删除了:
删除了: Earth
删除了:
删除了:
删除了: largely due to limitations in current altimetric retrieval frameworks to robustly obtain sea surface levels and ice surface heights, particularly across the pan-Arctic and throughout the seasonal cycle.
删除了:
删除了:
删除了:
设置了格式: 字体: 非倾斜
删除了: ~
删除了: ~0.7
删除了: The
删除了: 532 nm

Among the IS-2 products, ATL07 provides sea ice (snow-including) surface heights and surface types through a two-step height retrieval procedure and a fixed-threshold classification, applied to photon-aggregated segments containing approximately 150 photons (Kwok et al., 2023). As a key publicly available IS-2 sea ice product, ATL07 has been used in retrievals of sea ice freeboard, sea ice thickness and volume, ice-atmosphere drag coefficients, and linear ice fraction (Buckley et al., 2025; Koo et al., 2025; Kortum et al., 2025; Kwok et al., 2021; Mchedlishvili et al., 2023; Petty et al., 2020). Nevertheless, several limitations associated with its surface-height retrieval and surface-type classification approach constrain its performance, particularly for high-resolution retrievals and robust seasonal applications (Petty et al., 2020, 2023; Ricker et al., 2023). First, ATL07 signal extraction can be affected by detector after-pulses, i.e., delayed artificial photon events that occur after strong surface returns and appear at predictable height offsets below the primary signal. These after-pulses are particularly relevant during saturation events over specular leads and can occasionally introduce biases in surface-height retrieval (Farrell et al., 2020; Lu et al., 2021). Second, ATL07 uses variable segment lengths to accumulate sufficient signal photons (approximately 150) for precise surface-height retrieval, particularly over flat lead surfaces used for sea-surface referencing. This precision-oriented design is well suited for stable lead-height retrieval, but it can also smooth fine-scale ice morphology when segment lengths become long (10-200 m for strong beams; 40-800 m for weak beams), thereby reducing the ability of ATL07 to resolve ridge-related height variations to some extent (Duncan and Farrell, 2022; Ricker et al., 2023). Third, the fixed-threshold classification is sensitive to surface heterogeneity during the melt season (Tilling et al., 2020), when melt ponds and wet snow diminish the contrast in radiometric signatures, increasing lead misclassification (Kwok et al., 2016; Liu et al., 2025). Since freeboard retrieval relies on accurate identification of leads to estimate local sea level, such misclassifications can propagate directly into freeboard uncertainties. Furthermore, IS-2 weak-beam observations have so far been utilized and evaluated less extensively for freeboard retrieval owing to their lower transmitted energy, although they have been applied successfully to determine dust-storm heights and to derive terrain profiles in mountainous regions (Dandabathula et al., 2025; Zhang et al., 2021). Theoretically, the IS-2 weak-beam observations can increase the actual area of sensed sea ice (Ricker et al., 2023).

Notably, recent research has increasingly focused on developing specialized algorithms that use raw ATL03 photon data. For surface-height retrieval, the University of Maryland Ridge Detection Algorithm (UMD-RDA) improves ridge identification from ATL03 (Duncan and Farrell, 2022; Farrell et al., 2020), but it does not provide the surface type classification required for freeboard estimation. While upcoming updates to the ATL07 product aim to adopt 10-m fixed-length segments and non-Gaussian distributions (Wimert et al., 2025), they still rely on the original classification approach. Specialized melt-season algorithms, such as DDA-Bifurcate-Sea-ice, have succeeded in detecting melt ponds on multi-year ice (Buckley et al., 2023; Herzfeld et al., 2023), but they do not distinguish between ice floes and leads. For surface-type classification, machine-learning classifiers have improved lead detection (Koo et al., 2023; Liu et al., 2025), but they remain structurally tied to ATL07's preprocessing frameworks, which precludes direct application to ATL03 photon data. Although substantial progress has been made, existing efforts typically target individual subtasks rather than integrating them within a photon-level processing pipeline. Without a unified photon-level approach, uncertainties can propagate across steps and the methodology

删除了: ~
删除了: the only
删除了:
删除了:
删除了:
删除了: /
删除了: First, the ATL07 signal extraction is susceptible to detector after-pulses during saturation events, which frequently occur over specular leads, occasionally inducing biases in surface height
删除了: the variable segment lengths
删除了: –
删除了: –
删除了: smooth fine-scale ice morphology
删除了: resulting in underestimation of freeboards, surface roughness, and ridge heights
删除了: systematic
删除了: In terms of the
删除了: Furthermore, f
删除了: While

becomes difficult to generalize across varying seasonal states and surface regimes. Consequently, high-resolution freeboard retrieval that is reliable under both winter and summer conditions and transferable across surface types and beam types remains challenging.

删除了: year-round

In this study, we introduce the High-Resolution Freeboard Method (HRFM), a framework that retrieves sea-ice freeboard directly from ATL03 photon data and is designed for both strong- and weak-beam observations under winter and summer surface conditions. HRFM incorporates two key advances to address the aforementioned limitations: 1) A refined surface-height retrieval algorithm employing a two-stage denoising strategy, combining Kernel Density Estimation (KDE) with adaptive histogram-based filtering. This approach enables robust signal extraction at the native 0.7-m photon scale, preserving fine-scale morphology even under high solar background and during melt-season ice conditions. 2) A machine-learning surface-type classifier trained on 25 coincident Sentinel-2 (S2) /ICESat-2 scenes acquired in winter and summer, spanning approximately 200 000 km² and encompassing both multi-year and first-year ice under level and deformed conditions. This classifier ensures seasonally consistent lead identification, which is critical for accurate local sea-level estimates. By integrating these components, HRFM provides along-track freeboard estimates at 5-m intervals and gridded freeboard fields across seasons.

删除了:

删除了: maintains consistent performance for both strong and weak beams throughout the year.

删除了:

删除了: ~

The structure of this study is as follows: The datasets and methods are described in **Sect. 2** and **Sect. 3**, respectively. **Section 4** presents the retrieval results and validation. **Section 5** discusses the results, and Sect. 6 summarizes the main conclusions.

2 Data

This study focuses on the pan-Arctic sea-ice region, defined as areas where the monthly sea-ice concentration (SIC) exceeds 50%. This threshold was applied to exclude most isolated ice features near the ice edge, as they can contaminate the signal and significantly degrade satellite retrievals of sea-ice freeboard, owing to strong ice and oceanic dynamics (Kwok et al., 2023). The magenta line in **Figure 1** denotes the 50 % SIC contour derived from the multi-year mean April SIC during 2019–2023.

删除了:

删除了: by

删除了:

删除了:

删除了: pink

删除了: ,

删除了: for

删除了: (**Fig. 1**).

设置了格式: 字体: 加粗

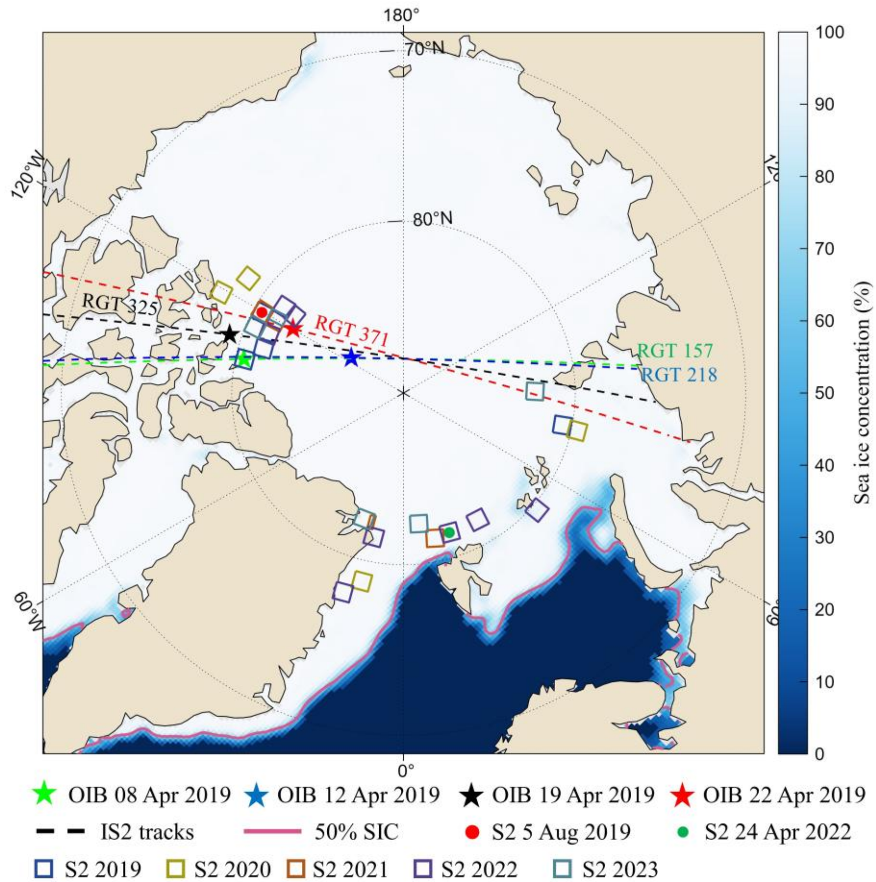

Figure 1. Overview of the study area and multi-source datasets. The background shading shows the mean April monthly SIC during 2019-2023 from the NOAA Climate Data Record (CDR). The magenta contour represents the multi-year mean April 50% SIC. The dashed lines mark ICESat-2 Reference Ground Tracks (RGT) 157, 218, 325, and 371, with the green, blue, black, and red stars indicating the location of coincident Airborne Topographic Mapper (ATM) measurements. Colored squares denote Sentinel-2 (S2) images from 2019-2023 that spatially coincide with ICESat-2 profiles and were used for training and validation. The red and Green dots show the positions of the Sentinel-2 scenes detailed in Sect. 3.2.1

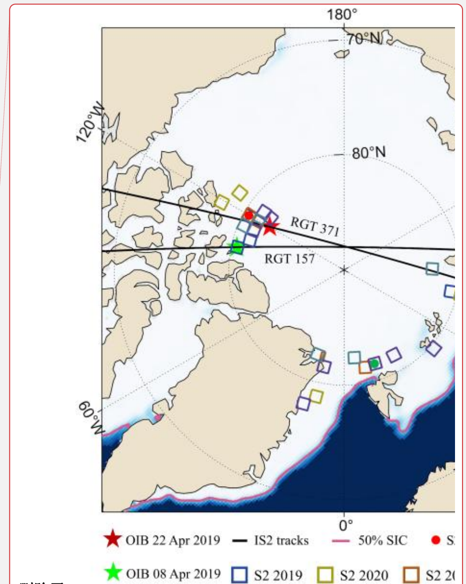

删除了:

删除了: :

删除了: obtained in

删除了: –

删除了: pink

删除了: black

删除了: 371 and 157,

删除了: and green

删除了: , obtained from years of 2019 – 2023

删除了: R

删除了: image

2.1 ICESat-2 data

ICESat-2 (IS-2) provides a suite of sea ice products derived from its photon-counting lidar observations. The processing workflow begins with geolocated photon clouds (ATL03), progresses to segment-level surface heights and surface-type classifications (ATL07) and along-track freeboard estimates (ATL10), and culminates in gridded monthly freeboard product (ATL20). In this study, HRFM uses ATL03 (Version 6) as the primary input to retrieve surface height, surface type, and freeboard (**Sect. 3**). ATL07 (Version 6) and ATL20 (Version 5) are used for comparison and evaluation purposes (**Sect. 4**). Although the newer ATL07 release (Version 7) introduces fixed 10 m segment lengths, it was experimental and limited to strong-beam observations during the study period. Therefore, to ensure a consistent and comprehensive evaluation across both strong and weak beams, ATL07 (Version 6) is used as the comparison reference unless otherwise specified.

2.1.1 ATL03 global geolocated photon data

The ATL03 product provides geolocated and time-tagged photon events detected by ATLAS (Neumann et al., 2023). Each photon is associated with its latitude, longitude, ellipsoidal height, photon confidence label, background rate estimates, and geophysical corrections, including corrections for tidal, atmospheric and inverse barometer effects. The photon heights are referenced to the WGS-84 ellipsoid. In HRFM, these corrections are applied to derive the corrected height for each photon.

2.1.2 ATL07 sea ice height

The ATL07 product provides sea ice surface heights and surface-type classifications derived from ATL03 photon data for estimating sea ice freeboard (Kwok et al., 2023). In this product, raw photons are aggregated into adaptive segments containing approximately 150 siganl photons, resulting in variable along-track lengths ranging from 10–200 m for strong beams to 40–800 m for weak beams (Kwok et al., 2019b). Surface height estimation involves a two-stage trimming process: 1) removing photons outside a fixed height window (−2.0 m to 3.5 m) and 2) excluding photons beyond two standard deviations of the remaining photons. A dual-Gaussian distribution is then assumed to fit the trimmed histogram to derive the segment's surface height (Kwok et al., 2023).

Surface type is classified using empirical thresholds based on photon rate, background rate, and the width of the photon distribution, informed by Multiple Altimeter Beam Experimental Lidar (MABEL) measurements and post-launch IS-2 assessments (Petty et al., 2021; Kwok et al., 2016). The classified categories include (-1) unknown surface type, (0) cloud covered, (1) non-lead snow/ice surface, (2-5) specular lead, and (6-9) dark lead, denoted by the *height_segment_type* flag. Specular (dark) lead segments are leads with high (low) photon rates. To mitigate uncertainties in radiometric classification, ATL07 applies a post-classification height filter using neighboring specular lead segments within a 10-km window. A candidate lead's height must lie between the minimum of the specular lead heights (h_{sl_min}) and the larger of (i) the 2nd percentile of specular lead heights, or (ii) $h_{sl\_min} + 2\sigma$, where $\sigma = 0.02$-0.03 m is the expected surface-height uncertainty over

删除了: our
删除了: utilizes
删除了: 0
删除了: 0
删除了: 0
删除了: release
删除了: 0
删除了: we use A
删除了: V06
设置了格式: 字体: (中文) +中文正文 (宋体), (中文) 简体中文(中国大陆)
删除了: ,
删除了:
删除了:
删除了: those
删除了: ,
删除了: all referenced to the WGS-84 ellipsoid.
删除了: our
删除了:
删除了:
删除了: (Kwok et al., 2023)
删除了:
删除了: -
删除了: ~
删除了: ~
删除了:
删除了: ,
删除了: s
删除了: height
删除了: C
删除了: utilizing
删除了: –

specular-lead segments. Segments meeting both classification and height-filter criteria are flagged as *ssh_flag* = 1, designating them as potential sea surface segments for ATL10 and ATL20 freeboard estimations.

2.1.3 ATL20 gridded sea ice Freeboard

The ATL20 product provides basin-scale Arctic sea-ice freeboard fields as daily and monthly composites on a 25 km × 25 km polar stereographic grid. These gridded fields are derived from along-track ATL10 freeboard estimates using only strong-beam observations (Kwok et al., 2023). To ensure data quality and minimize coastal or open-ocean contamination, ATL20 applies a strict mask, retaining grid cells only where the SIC exceeds 50% and the distance from the coastline is at least 25 km. In this study, monthly freeboard fields derived from HRFM are compared with the ATL20 from October 2021 to September 2022 to evaluate their basin-scale spatial consistency during the one-year demonstration period..

2.2 Sentinel-2 data

To construct a robust training dataset for the machine-learning surface-type classifier, we selected Sentinel-2A and -2B scenes near-coincident with IS-2 overpasses during 2019 – 2023. A maximum time offset of 30 min was applied to minimize misregistration due to sea-ice advection, while retaining a sufficient number of coincident observations. Assuming a typical sea ice drift speed of approximately 0.05–0.1 m/s, a 30-min offset corresponds to an advective displacement of approximately 90–180 m. This displacement is small relative to the spatial extent of a Sentinel-2 scene, approximately 290 km × 290 km, and can be further reduced by manual alignment based on correspondence between surface optical features and IS-2 photon returns. Because of Sentinel-2's orbital inclination, coincident acquisitions are limited to latitudes south of 82° N.

From an initial pool of 822 overlapping scenes spanning 416 IS-2 tracks, we applied a stringent quality-control procedure. Each scene was manually interpreted using true-color imagery to identify surface types. Leads were distinguished from ice floes based on their characteristic elongated morphology and low reflectance in the visible bands. After extensive manual review, 25 scenes corresponding to 25 IS-2 overpasses were retained as the training and validation dataset. These scenes cover multiple Arctic regions, seasons, sea-ice types, and surface-roughness conditions, with their locations shown in **Figure 1**. Their file names, acquisition dates, and time offsets are summarized in Table A1.

2.3 ATM data

The performance of HRFM in retrieving high-resolution along-track heights was evaluated using coincident observations from the Airborne Topographic Mapper (ATM), collected during dedicated IS-2 underflights of NASA's Operation IceBridge (OIB) on April 2019 (Kwok et al., 2019a). The ATM uses a conically scanning green laser lidar (532 nm) that produces footprints approximately 1 m in diameter with a vertical precision of approximately 0.03 m (Krabill et al., 2002). We used ATM profiles from four OIB underflights acquired on 8, 12, 19, and 22 April 2019. These underflights were coincident with IS-2 RGTs 157, 218, 325, and 371, respectively, as shown by the green, blue, black, and red stars in **Figure 1**. The four ATM underflights

删除了: The ATL20 product provides a basin-scale perspective of Arctic sea ice freeboard, offering daily and monthly composites on a 25 km × 25 km polar stereographic grid.
删除了: These gridded fields are derived from along-track ATL10 freeboard estimates exclusively using strong-beam observations
删除了: product for the period
删除了:
删除了:
删除了: ~
删除了: 150
删除了: ,
删除了: which is negligible relative to the spatial extent of a single Sentinel-2 scene (~290 km × 290 km) and is easy to align them manually…
删除了: (
删除了:)
删除了: The retained
删除了: a wide range of Arctic regions (~200 000 km²), sea ice types, surface-roughness conditions, and seasons, supporting the classifier's applicability (locations marked in
删除了: **Fig. 1**
删除了:)
设置了格式: 字体: 加粗
删除了: is
删除了: also
删除了: a
删除了: utilizes
删除了: ~
删除了: two
删除了: acquired within ~38 min of coincident IS-2 tracks.
删除了: There are ~149 km of along-track overlap below IS-2 reference ground track (RGT) 157 and ~187 km of along-track overlap below IS-2 RGT 371 (green and red stars in
删除了: **Fig. 1**
删除了:)
设置了格式: 字体: 加粗

provide independent elevation references for assessing HRFM-derived surface heights and the preservation of fine-scale sea-ice features. Because the degree of spatial overlap and temporal separation differs among the four flights, the ATM comparison statistics are interpreted under the specific collocation described in Sect. 4.1.

3 Method

This section details the implementation of the HRFM for ATL03 photon data. As illustrated in **Figure 2**, HRFM consists of two main components. The first component is high-resolution surface height retrieval, which begins with a two-stage denoising procedure designed to remove background photons and detector after-pulses while preserving morphology-related surface photons as faithfully as possible. The filtered signal photons are subsequently used to estimate surface heights within fixed 5-m along-track segments. The second component is surface-type classification, in which ATL03-derived segment features are interpreted with the aid of coincident Sentinel-2 imagery and used to train a machine-learning classifier. The resulting lead classification provides the local sea-surface reference required for freeboard retrieval.

删除了: These dense, independent elevation surveys provide the primary reference for assessing the accuracy of HRFM-derived surface heights and the preservation of fine-scale sea ice features.

删除了: applied to

删除了: in the schematic workflow

删除了: **Fig. 2**

删除了: the method

设置了格式: 字体: 加粗

删除了: a

删除了:

删除了: that removes background and after-pulse photons while preserving morphology-related photons as faithfully as possible.

删除了: -length

删除了: The second component is a machine-learning surface-type classifier that discriminates between ice floes and leads, facilitating the estimation of reference sea level required for freeboard retrieval.

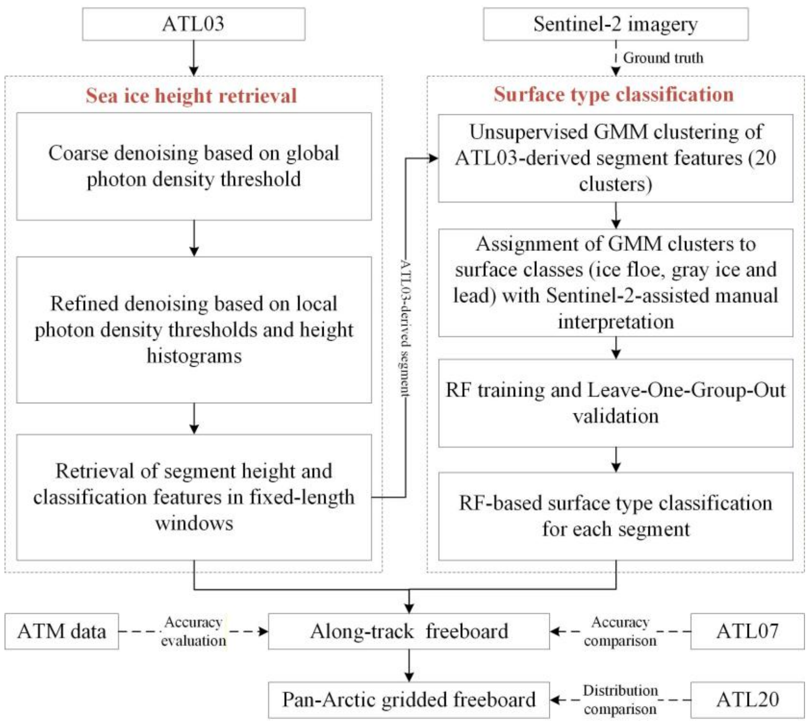

Figure 2. The flowchart of HRFM.

Compared to the ATL07 algorithm, HRFM introduces two main advancements. First, photon-density information is incorporated into both surface-height retrieval and surface-type classification, improving robustness under challenging conditions, such as high solar background, detector saturation, and melt-affected surfaces. This improves the retention of sea ice morphology-related photons, particularly over ridges, narrow leads, and melt ponds, and supports denser surface-height sampling. Second, HRFM uses a machine-learning classifier trained from coincident Sentinel-2 imagery, rather than relying solely on fixed empirical thresholds. This data-driven approach improves the discrimination of sea ice and leads under different seasonal surface conditions, particularly during the melt season when surface radiometric contrast is reduced.

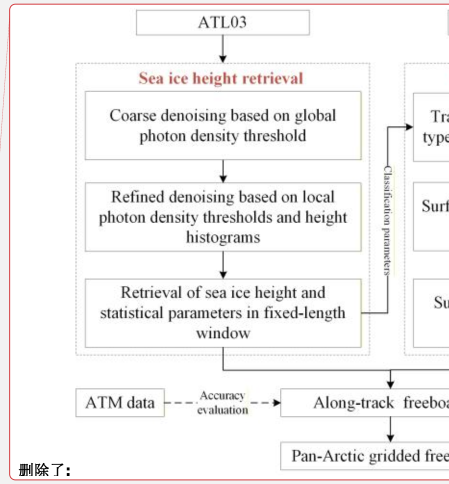

删除了:

删除了: :

删除了: provides

删除了: major

删除了: including ATLAS detector saturation and footprints affected by melt ponds.

删除了: yields more accurate surface height estimates and denser freeboard sampling

删除了: This improvement is especially pronounced for weak beams, where lower transmitted energy and reduced signal-to-noise ratios often degrade ATL07 retrieval performance.

删除了: employs

删除了: the empirical thresholds used in ATL07

删除了: This approach provides more reliable and seasonally consistent discrimination of sea ice features, particularly during the melt season when surface radiometric contrast is reduced.
This facilitates the continuous and stable acquisition of reference sea level.…

3.1 Surface height retrieval

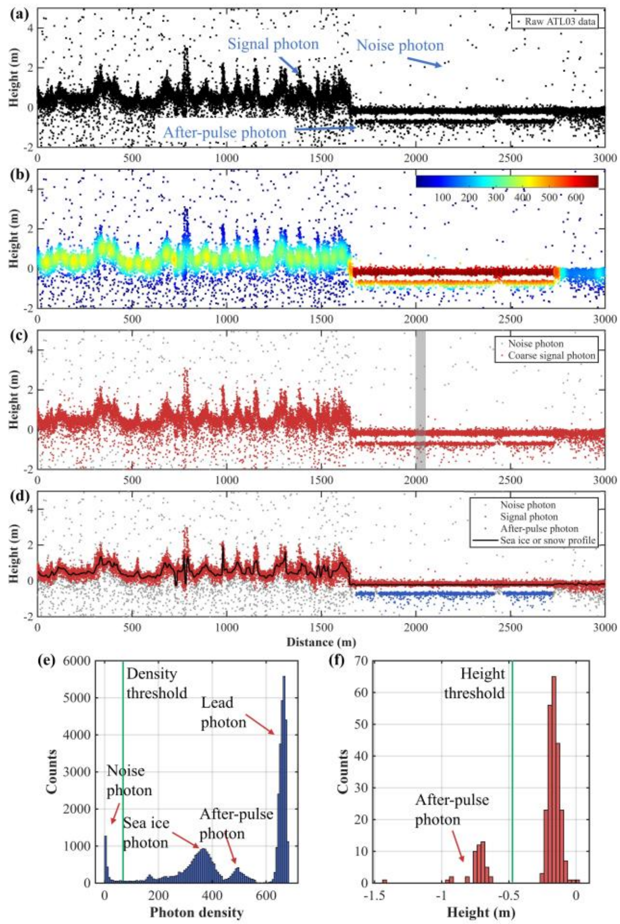

Figure 3. Sequential processing steps for retrieving sea ice surface height from the middle strong beam of ATL03_20190526002946_08820304_006_02 obtained over the Lincoln Sea. (a) Raw ATL03 data converted into distance height coordinates. (b) KDE-estimated photon density (the color bar indicates photon density). (c) Coarse signal photons after density-thresholding and local height-window filtering.. (d) Refined signal photons, together with the detected after-pulse photons and the retrieved sea ice or snow surface profile at 5-m along-track resolution. (e) Histogram of photon density corresponding to panel (b). The green vertical line indicates the density threshold used to separate noise photons from coarse signal photon. (f) Height histogram of coarse signal photons within the grey-shaded region in panel (c). The green vertical line denotes the height threshold applied to distinguish after-pulse photons from surface signal photons.

删除了: :
删除了:
删除了: from
删除了: of the Arctic Ocean
删除了: along-track
删除了: –
删除了: retrieved
删除了: horizontal resolution
删除了:

As illustrated in **Figure 3a**, accurate surface height retrieval from ATL03 data requires the separation of signal photons (surface) from noise photons (background) originating from solar background, atmospheric scattering, and detector dark counts. HRFM implements a two-stage denoising strategy, consisting of coarse and refined filtering, to extract the final set of signal photons. The resulting signal photon set forms the basis for surface height retrieval at fixed 5-m segments. The summary of key algorithm parameters used in HRFM is listed in Table A2.

3.1.1 Coarse denoising

To remove large-scale background noise, raw ATL03 photons are first divided into 3-km along-track segments. Their heights are referenced to the DTU21 Mean Sea Surface (MSS) model (Andersen et al., 2023) to remove geoid trends. Photon density is calculated using a KDE approach. For each photon *p*, the density D_p is defined as:

$$D_p = \sum_{i=1}^{n} K(d_{pi}), \tag{1}$$

where *n* is the number of photons within a predefined search region, d_{pi} is the distance between photon *p* and neighbor photon *i*, and *K* is kernel function (Chu et al., 2017):

$$K(d_{pi}) = \frac{3}{4}\max(0, 1 - d_{pi}^{\ 2}). \tag{2}$$

Since ATL03 photons show much stronger clustering in the horizontal direction than in the vertical direction, distances are computed within an anisotropic elliptical search region:

$$d_{pi} = \sqrt{\frac{\Delta x_{pi}^{\ 2}}{a^2} + \frac{\Delta h_{pi}^{\ 2}}{1}}, \tag{3}$$

where Δx_{pi} and Δh_{pi} represent the distances between the two photons in the horizontal and vertical directions, respectively. The horizontal scaling parameter *a* is set to 25 for strong beams and 100 for weak beams. This process is used to increase the weight of photons in the horizontal direction, thereby preserving the along-track resolution and improving signal-photon extraction (Lu et al., 2025).

Photon densities vary along track due to differences in surface types and beam types (**Figure 3b, Figure A1b**, and **Figure A2b**). To determine a segment-specific threshold that removes noise while retaining morphology-related photons (e.g. ridges or melt ponds), we examine the photon-density distribution within each 3-km segment. The resulting density histogram typically shows a multi-modal structure (**Figure 3e, Figure A1e, and** Figure A2**e)** corresponding to various ground object features: 1) a narrow low-density peak representing noise photons, 2) a broad intermediate-density peak corresponding to sea ice photons, 3) a smaller secondary peak linked to after-pulse photons or weak subsurface scattering, and 4) a high-density peak associated with specular leads.

删除了: Fig. 3
删除了:
设置了格式: 字体: 加粗
删除了: noise
删除了: denoising
删除了:
删除了: raw
删除了: Fig. 3
删除了: Fig. A1
设置了格式: 字体: 加粗
设置了格式: 字体: 小五, 加粗
设置了格式: 字体: 小五, 加粗
域代码已更改
域代码已更改
删除了: Fig. A2
删除了: Fig. 3
删除了: Fig. A1
删除了: Fig. A2
设置了格式: 字体: 加粗
设置了格式: 字体: 小五, 加粗
域代码已更改
域代码已更改

We fit the noise and sea ice peaks using a two-component Gaussian mixture model (GMM). The intersection of the two fitted components defines the segment-specific density threshold (green lines in **Figure 3e**, **Figure A1e**, and **Figure A2e**). Photons with densities exceeding this threshold are retained as coarse signal photons (**Figure 3c**, **Figure A1c**, and **Figure A2c**). The retained coarse signal photons are then further constrained by a local height window, from 2 m below to 6 m above the modal height within each 3 km along-track segment. However, some after-pulse photons and subsurface returns can overlap in density with the sea ice signal; therefore, a second local refinement step is required.

3.1.2 Refined denoising

The retained coarse signal photons are further processed within local 10 m windows to remove residual background photons and detector after-pulses. This refinement step uses different filtering strategies depending on the ATLAS detector saturation state. Saturation is assessed using the signal photon rate, defined as the number of coarse signal photons per transmitted pulse within the local window. Based on ATLAS instrument characterization, detector saturation is identified when the photon rate exceeds 16 photons per pulse for strong beams or 4 photons per pulse for weak beams.

Under saturation conditions, after-pulse echoes can appear at fixed vertical offsets below the true surface, typically approximately 0.45 m and 0.9 m (Lu et al., 2021). Because these after-pulse photons can have densities comparable to surface-signal photons, density information alone can not reliably distinguish these photons. Therefore, a 0.1-m height interval histogram is constructed for each saturated window (**Figure 3f** and **Figure A1f**), and the primary peak is taken as the physical surface. Photons situated more than 0.3 m below this peak are classified as after-pulses and removed, as indicated by the green lines in **Figure 3f** and **Figure A1f**.

For non-saturated windows, remaining noise photons are removed using a locally adaptive density threshold. The threshold is set to the 10th percentile of coarse signal photon densities within the window. Only photons with densities exceeding this threshold are retained as refined signal photons. Together, the coarse and refined denoising stages isolate the final signal photons, as illustrated in **Figure 3d**, **Figure A1d**, and **Figure A2d**.

We note that the Yet Another Photon Classifier (YAPC) variables provided in recent ATL03 releases offer an additional density-like metric as well, which could be incorporated as an additional filtering variable in future versions of HRFM.

3.1.3 Sea-ice surface-height Estimation

Following refined denoising, surface heights are estimated from the final signal photon set. Although ATL03 provides photon-level observations at an along-track sampling interval of approximately 0.7 m, surface-type classification and freeboard retrieval require statistical estimates at the segment scale. Therefore, the along-track profile is partitioned into fixed 5-m segments after trade-off analyses between spatial resolution and height precision. For each segment, the surface height is defined as the KDE-density-weighted mean of all refined signal photon heights (black lines in **Figure 3d** and **Figure A1d**):

删除了: Fig. 3
删除了: Fig. A1
删除了: Fig. A2
设置了格式
设置了格式
设置了格式
域代码已更改
域代码已更改
删除了: Fig. 3
删除了: Fig. A1
删除了: Fig. A2
设置了格式
设置了格式
设置了格式
域代码已更改
域代码已更改
删除了: Refined denoising is performed within local 10-m window
删除了: ~….45 m and ~….9 m (Lu et al., 2021). Because these
删除了: Fig. 3
设置了格式
设置了格式
域代码已更改
设置了格式
删除了: Fig. A1…f), and the primary peak is taken as the physical
删除了: Fig. 3
删除了: Fig. A1…f)
设置了格式
设置了格式
域代码已更改
删除了: In the absence of saturation,
删除了: Fig. 3
删除了: Fig. A1
删除了: Fig. A2
设置了格式
设置了格式
设置了格式
域代码已更改
域代码已更改
删除了: …ce surface-
删除了: optimized…inal signal photon set. Although ATL03
删除了: Fig. 3
删除了: Fig. A1
设置了格式
设置了格式
域代码已更改

$$H_{seg} = \frac{\sum_{i=1}^{N} D_i \cdot h_i}{\sum_{i=1}^{N} D_i}, \quad (4)$$

where h_i and D_i are the corrected height and KDE-derived density of the i-th photon, respectively. Geophysical corrections, including tidal, atmospheric, and mean-sea-surface corrections, as well as the first-photon-bias correction (Kwok et al., 2026) were applied. The corrected segment height relative to the mean sea surface can be summarized as

$$H_{seg} = h_{03\_raw} - h_{set} - h_{sept} - h_{opt} - h_{ol} - h_{mss} - h_{ot} - h_{lpe} - h_{DAC} - h_{fpb} + h_{atm}, \quad (5)$$

Where h_{03_raw} is the 'uncorrected' photon height in ATL03, h_{set} is the solid earth tide correction, h_{sept} is the solid earth pole tide correction, h_{opt} is the ocean loading correction, and h_{ol} is the ocean pole tide correction, h_{mss} is the mean sea surface, h_{ot} is the ocean tide correction, h_{lpe} is the long period equilibrium tide correction and h_{DAC} is the dynamic atmospheric correction, h_{fpb} is the first-photon-bias computed using the system engineering tables supplied in the ATL03, h_{atm} is the atmospheric path delay range correction. The data source and application of each correction term are summarized in Table A3.

To support the subsequent machine-learning classification, four statistical parameters are extracted for each 5-m segment: (1) photon rate, defined as the number of refined signal photons per transmitted pulse and used as a proxy for relative surface brightness; (2) background rate, defined as the mean ATL03 background rate within the segment and used to represent scattered sunlight at the laser wavelength; (3) height standard deviation (STD), defined as the spread of refined signal photon heights within the segment and used to represent small-scale surface roughness; and (4) mean photon density, defined as the average KDE-derived photon density of the refined signal photons. Following ATL07, the background rate is normalized to a solar elevation angle of 20° (Kwok et al., 2023).

Furthermore, segments impacted by melt ponds are identified by adapting the bimodal height distribution analysis proposed by Herzfeld et al. (2023). A segment is flagged as melt-pond affected when (1) the photon rate remains below the saturation threshold and (2) the height histogram is bimodal, indicating returns from both the pond surface and the pond bottom (Figure A2). Although such subsurface returns may be useful for potential melt-pond depth retrieval applications (Buckley et al., 2023; Herzfeld et al., 2023), melt-pond-affected segments are excluded from the freeboard estimation to avoid introducing a downward height bias.

3.2 Surface-type classification

Accurate surface-type classification is a prerequisite for reliable freeboard retrieval, as the local reference sea level is determined from identified lead segments. In this section, we first analyze two representative winter and summer scenes using coincident Sentinel-2 imagery to examine the variability of the four HRFM classification parameters across various surface types. We then describe the construction of a labeled training dataset based on unsupervised clustering and visual interpretation.

删除了: geophysical
删除了: Geophysical corrections (e.g. atmospheric delays and tides)
删除了: are
删除了: .
域代码已更改
域代码已更改
域代码已更改
域代码已更改
域代码已更改
域代码已更改
域代码已更改
域代码已更改
域代码已更改
域代码已更改
域代码已更改
域代码已更改
删除了: we extract
删除了: features
删除了: Photon rate: the number of refined signal photons per transmitted pulse within a 5 m segment (a proxy for relative surface brightness).…
删除了: Background
删除了: :
删除了: the mean ATL03 background rate for all photons in the segment, indicative of scattered sunlight at the laser wavelength.
删除了: The background rate is normalized to a solar elevation an
删除了: Height standard deviation (STD): the spread of refined
删除了: Mean
删除了: : the average KDE-derived photon density (not available
域代码已更改
删除了: Fig. A2
删除了: While
删除了: these
删除了: can
删除了: preserved for potential depth retrieval applications
删除了: these
删除了: downward bias
删除了:
删除了:
删除了: exclusively
删除了: ,

Finally, we introduce the machine learning classifier employed in HRFM to discriminate between floe- and lead-dominated segments.

3.2.1 Variability of classification parameters

To characterize the responses of the four HRFM classification parameters across diverse surface types, we analyze two representative IS-2/S-2 coincident scenes: a winter case acquired in April 2022 (**Figure 4**) and a summer case affected by melt ponds in August 2019 (**Figure 5**). Each scene contains a strong/weak beam pair (gt3l and gt3r) to evaluate beam-dependent sensitivity. Based on the coincident Sentinel-2 imagery, the winter scene suggests visually identifiable snow-covered sea ice, thin young ice with little or no snow cover, and open-water leads (**Figure 4a**) whereas the summer scene is characterized by a mixture of open water, melt ponds, bare ice, and residual deteriorated snow (**Figure 5a**).

删除了: Sentinel
删除了: (April 2022,
删除了: **Fig. 4**
设置了格式: 字体: 小五, 加粗
删除了: featuring melt ponds (August 2019,
删除了: **Fig. 5**
设置了格式: 字体: 小五, 加粗
删除了: **Fig. 4**
设置了格式: 字体: 小五, 加粗
删除了: **Fig. 5**
设置了格式: 字体: 小五, 加粗

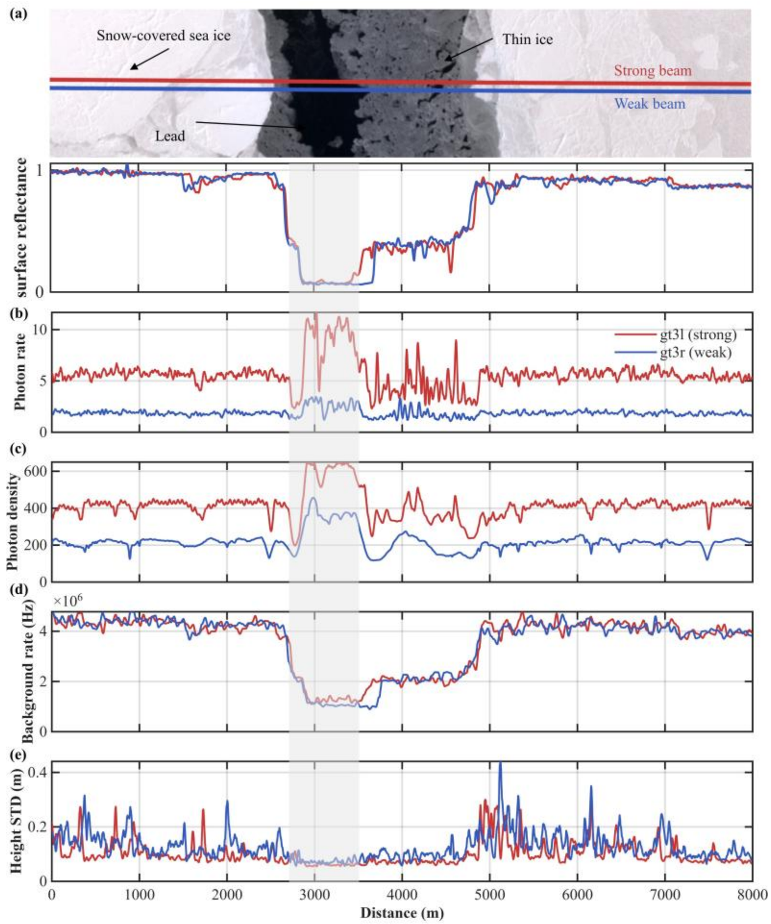

Figure 4. Winter case over an approximately 8 km along-track profile acquired on 24 April 2022. (a) Sentinel-2 RGB imagery (green dot in Figure 1) overlaid with ICESat-2 gt3l (strong beam, red) and gt3r (weak beam, blue), with surface reflectance derived from the RGB bands of the Sentinel-2 image from nearest neighbor pixels to the ICESat-2 segments. (b) Photon rate, (c) photon density, (d) background rate, and (e) height standard deviation (STD) along track. The gray-shaded region indicates the open-water lead area.

删除了: :

删除了: with an along-track profile of approximately 8 km acquired on 24 April 2022.

删除了: Fig. 1

删除了: d

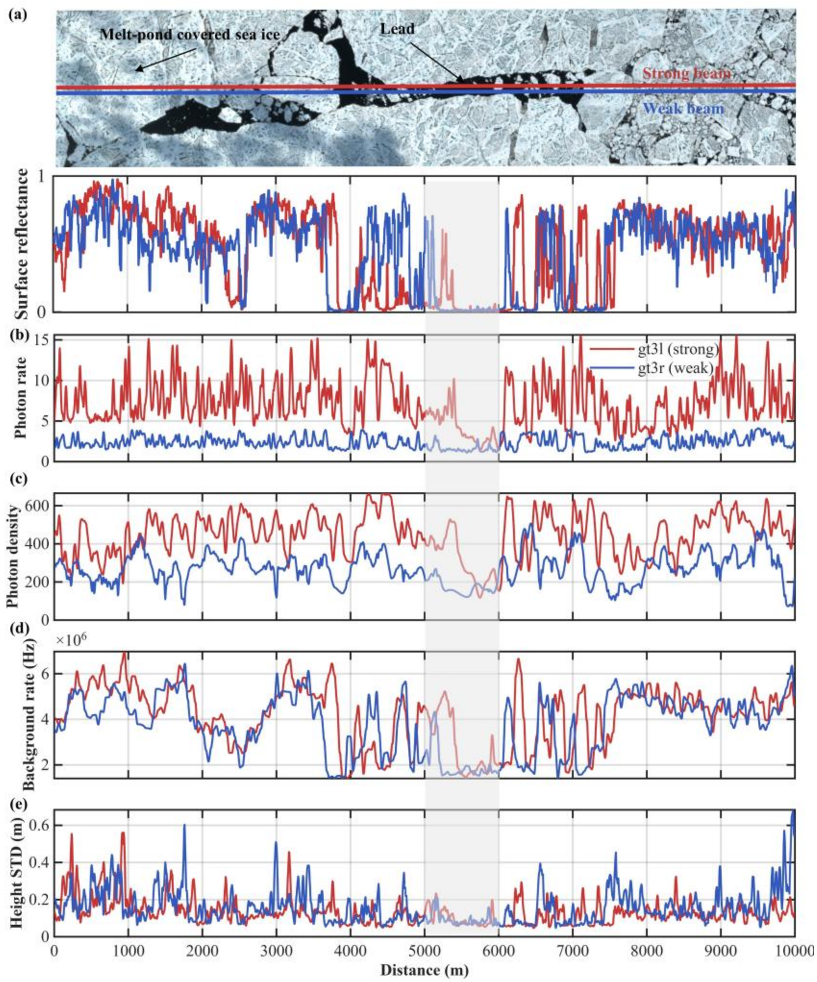

Figure 5. Same as Figure 4, but for an approximately 10 km along-track profile acquired on 5 August 2019 (red dot in Figure 1).

In the April (winter) scene, photon rate (**Figure 4b**) and photon density (**Figure 4c**) generally scale with Sentinel-2-derived surface reflectance over snow-covered and thin ice, yielding relatively stable along-track values. In contrast, pronounced localized spikes are observed over the lead region, where photon rates and photon densities exceed those over adjacent snow-

删除了: :
删除了: A
删除了: in
删除了: Fig. 4
删除了: I
删除了: t's a 10-km profile observed on 5 August 2019
删除了: Fig. 1
删除了: Fig. 4
删除了: Fig. 4
删除了: surface RGB
设置了格式: 字体: 小五, 加粗
设置了格式: 字体: 小五, 加粗
带格式的: 缩进: 左 0.5 字符, 首行缩进: 0.5 字符
删除了: and
删除了: consistently
删除了: s
删除了: often

covered ice. These enhancements result from strong specular reflections off smooth open-water or newly formed thin-ice surfaces, which concentrate a large fraction of the emitted laser energy back toward the receiver despite the low reflectance of water (**Figure 4a**). However, in the August (summer) scene, specular returns occur with higher frequency due to the widespread presence of melt ponds and narrow leads, resulting in substantially increased along-track variability in both photon rate (**Figure 5b**) and photon density (**Figure 5c**). Notably, the wide (approximately 1000 m) open-water lead, indicated by the gray shaded region at 5 – 6 km in **Figure 5**, shows simultaneously low photon rate and photon density, unlike the winter case, suggesting a rougher (likely wind-roughened) water surface that scatters energy away from the receiver. This may be related to stronger wind-driven surface waves in summer open water relative to winter conditions (Liu et al., 2016) or the absence of new ice formation in leads compared to the winter case where new ice forms rapidly and truly open water will rarely be present. Across both scenes, weak beams exhibit a reduced dynamic range and diminished contrast, complicating the discrimination between classes. Figure A5 shows the monthly distributions of photon rate and photon density across the annual cycle, further indicating their seasonal difference.

The background rate is predominantly influenced by solar illumination geometry and surface reflection. Its along-track variation closely tracks the intensities in Sentinel-2 RGB imagery and is nearly identical between strong and weak beams (**Figure 4d** and **Figure 5d**), reflecting their shared dependence on solar background. Background rates are highest over bright snow-covered ice (4–5 MHz), intermediate over thin ice (2–3 MHz), and lowest over dark open-water leads (1–2 MHz), qualitatively matching the strong albedo contrast from snow-covered sea ice (0.7–0.8) to open water in leads (0.1–0.2) (Light et al., 2022). In the summer scene, background rate variations increase because melt ponds, bare ice, and wet snow mix over much shorter spatial scales with high spatial heterogeneity in the proportion among components within a single segment.

The height standard deviation reflects local surface roughness and shows a smaller dynamic range than the other parameters (**Figure 4e** and **Figure 5e**). It is higher and more spatially variable over deformed, snow-covered ice, but reduced over thin ice and leads, consistent with their smoother surface conditions.

In summary, while these four parameters provide complementary information for distinguishing sea ice from leads, consistent with early airborne photon-counting lidar studies (Kwok et al., 2016), their responses are highly sensitive to seasonal surface conditions, beam energy, and wind-induced roughness of open water surface, and ice type or age. The resulting nonlinear overlap in feature space motivates the use of a supervised, data-driven classifier for robust surface-type discrimination under both winter and summer conditions.

3.2.2 Training dataset generation

To develop a robust machine-learning surface type classifier, a high-quality labeled dataset was constructed using coincident Sentinel-2 imagery as the ground truth. Given that HRFM generates thousands of 5-m segments per overlapping scene, direct manual annotation of individual segments is impractical. Following the strategy previously developed for improving ATL07 classification (Liu et al., 2025), we combined unsupervised clustering with visual interpretation to generate the training dataset.

删除了: **Fig. 4**
设置了格式: 字体: 小五, 加粗
删除了: **Fig. 5**
删除了: **Fig. 5**
删除了: ~
设置了格式: 字体: 小五, 加粗
设置了格式: 字体: 小五, 加粗
删除了: **Fig. 5**
设置了格式: 字体: 小五, 加粗
删除了: **Fig. A4**
删除了: **Fig. 4**
删除了: **Fig. 5**
设置了格式: 字体: 小五, 加粗
设置了格式: 字体: 小五, 加粗
删除了: gray
删除了: ~
删除了: ~
删除了: **Fig. 4**
删除了: **Fig.5**
设置了格式: 字体: 小五, 加粗
设置了格式: 字体: 小五, 加粗
设置了格式: 字体: 加粗
删除了: transitions
删除了: s
删除了: s
删除了: s
删除了: This complex, nonlinear overlap in feature space motivates the use of a supervised, data-driven classifier to achieve robust and seasonally consistent surface type discrimination.
删除了: training

For each coincident IS-2/S-2 scene, HRFM segments were grouped into 20 clusters using a GMM applied to the four classification parameters of photon rate, background rate, height standard deviation, and photon density. This clustering step collapses a large number of segments into a limited number of statistically consistent groups, thereby reducing annotation effort while enhancing labeling robustness. Strong and weak beams were clustered independently because of their different photon statistics.

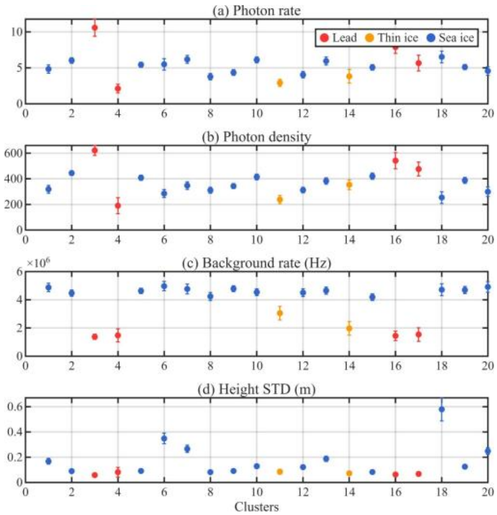

Figure 6. Mean values and standard deviations of the four classification parameters for clusters derived from ICESat-2 observations on 24 April 2022 (the winter case). Panels show (a) photon rate, (b) photon density, (c) background rate, and (d) height standard deviation (STD). The surface types are color-coded as lead (red), thin ice (yellow), and sea ice (blue).

Since the unsupervised clustering itself does not reveal surface type, each cluster was assigned a label using Sentinel-2 RGB imagery. Following the same visual interpretation criteria and alignment method for Sentinel-2 and IS-2 as in our earlier ATL07 work (Liu et al., 2025), the clusters were manually assigned to three surface types: sea ice, thin ice, and leads.

Figure 6 illustrates the mean values and standard deviations of the classification parameters for clusters derived from a representative strong-beam data on 24 April 2022. The clusters align with the expected parameter behaviors summarized in **Sect. 3.2.1**, indicating that they map consistently onto physical surface types. Sea ice clusters are characterized by high background photon rates and larger height standard deviations. Thin-ice clusters exhibit intermediate photon rates, photon densities, and background rates, with moderate height variability. Lead clusters are distinguished by either very high photon rates and densities associated with specular returns or very low photon rates and densities associated with dark leads, together with low background rates and small height standard deviations.

删除了: entinel

删除了: vast segment populations

删除了: :

带格式的: 两端对齐, 缩进: 首行缩进: 1 字符

删除了: (gray ice)

设置了格式: 字体: 小五, 加粗

删除了: Figure 6

设置了格式: 字体: 加粗, 不检查拼写或语法

设置了格式: 字体: 加粗

删除了: Lead clusters are distinguished by either extreme high (specular) or low (dark) photon rates and densities, accompanied by low background rates and height standard deviations.

For freeboard retrieval, misclassifying non-lead surfaces as lead segments is more problematic than the opposite case, because false lead detections can bias the local sea-surface reference and subsequently propagate into the freeboard estimates. Therefore, clusters were assigned to the lead class only when they appeared as clearly dark, open-water-like features in Sentinel-2 imagery and were consistent with the local ATL03 photon characteristics. Ambiguous surfaces were not labelled as leads unless they could be confidently interpreted as open-water leads.

Several transitional surface types remain difficult to separate using the available optical information. Therefore, the thin-ice class is used as a broad category that includes visually similar transitional ice types, such as nilas, frazil ice, and slush ice. In addition, melt-pond-covered ice clusters was conservatively treated as sea ice class, even when the ponds appeared dark in Sentinel-2 imagery. This choice was made to avoid misclassifying melt ponds as leads and incorrectly using them as sea-surface reference points in the freeboard retrieval. It should be noted that the manual labeling inevitably introduces some subjectivity and classification uncertainty, especially for transitional or ambiguous surface types.

This labeling process was applied consistently to 25 coincident IS-2/S-2 scenes shown in Figure 1, representing a wide distribution across the Arctic and a multi-year temporal range from 2019 to 2023. The final aggregated dataset comprises 1,029,289 labeled strong-beam segments and 1,023,895 labeled weak-beam segments, providing a substantial and diverse foundation for training the machine-learning classifier.

删除了: Sentinel-2/IS-2

删除了: **Fig.** 1

带格式的: 缩进: 首行缩进: 1 字符

删除了: temporal spread (2019–2023).

3.2.3 Training of machine learning classifier

With the labeled training dataset established, a supervised Random Forest (RF) classifier is employed to assign surface types to each HRFM segment. Consisting of an ensemble of decision trees, the RF algorithm is well-suited for this application due to its ability to capture complex, non-linear relationships among physical parameters without requiring feature normalization (Breiman, 2001). RF is computationally efficient and has been widely adopted in studies on sea ice classification (Fredensborg Hansen et al., 2021; Mugunthan et al., 2023; Shen et al., 2017). Furthermore, the ensemble-averaging nature of RF could mitigate sensitivity to mislabeling within the training data, which is unavoidable when surface labels are derived from Sentinel-2-assisted visual interpretation of statistically aggregated clusters.

删除了: visual interpretation of statistically aggregated clusters of samples from optical imagery

The RF classifier was configured with 200 decision trees and a maximum tree depth of 20 to ensure a balance between model complexity and computational efficiency. Separate models were trained for strong and weak beams to account for their distinct signal-to-noise ratios and dynamic ranges. The classification relies on the four primary features: photon rate, background rate, height standard deviation, and mean photon density. Previous studies indicated that photon rate and mean photon density provide the highest discriminative power for detecting specular leads, while background rate is crucial for separating thin ice from snow-covered ice (Koo et al., 2023; Kwok et al., 2016; Liu et al., 2025).

To ensure robust generalization across diverse spatial and seasonal conditions, we implemented a Leave-One-Group-Out (LOGO) cross-validation strategy. In each iteration, data from one entire coincident IS-2/Sentinel-2 pass was held out for testing, while the remaining 24 scenes were used for training. This rigorous approach prevents spatial autocorrelation from overinflating accuracy estimates and ensures the model can handle unseen geographical regions.

The trained classifier assigns a surface type of sea ice, thin ice, or lead to every HRFM segment. Segments previously identified as melt-pond influenced (details in Sect. 3.1.3) are excluded prior to classification to avoid ambiguity during the melt season.

Two classification settings were evaluated. First, a three-class classifier was trained to distinguish sea ice, thin ice, and lead, allowing the separability of transitional ice types to be assessed. Second, for the final freeboard retrieval, a conservative binary classifier was used in which thin ice was merged into the sea-ice class. This binary setting reduces the risk of using uncertain thin-ice segments as lead segments for local sea-surface reference construction. After the LOGO evaluation, the final binary RF classifiers for strong and weak beams were trained using all 25 labeled scenes and applied to the full HRFM dataset.

3.3 Sea ice freeboard estimation

Following surface-height retrieval and surface-type classification, HRFM derives freeboard at two spatial scales: along-track freeboard and monthly gridded freeboard fields.

(1) Along-track freeboard calculation

The along-track freeboard is computed by subtracting a local sea-surface reference from the heights of identified sea-ice segments. As the optimization of the local sea-surface reference is not the primary focus of this study, a pragmatic and efficient approach is adopted. Specifically, all lead segments identified within each 10-km along-track window are aggregated to estimate the local sea-surface height. To reduce the influence of spurious lead detections, lead heights falling outside three standard deviations of the window mean are excluded. The mean height of the remaining lead samples is then used as the local sea-surface reference for that window. In 10-km windows without valid lead detections, the local sea-surface reference is estimated by linear interpolation between the neighboring 10-km windows to ensure continuity.

(2) Gridded monthly freeboard

To generate composite maps of the Arctic freeboard and facilitate direct comparison with the ATL20 product, monthly gridded freeboard fields are generated on a 25-km polar stereographic grid (EPSG:3411). All valid along-track freeboard observations acquired within a given month are projected onto this grid. For each grid cell, the freeboard value is computed as a distance-weighted average of all contributing observations. Grid cells with no valid observations during the month are left empty.

4 Results

4.1 Surface height evaluation and comparison

To quantitatively evaluate the surface-height retrieval performance of HRFM and compare it with ATL07, we used coincident ATM observations within approximately 10 km along-track segments. ATM and ICESat-2 profiles were directly collocated without applying the cross-correlation maximization procedure used by Kwok et al. (2019a). Before comparison, HRFM, ATL07, and ATM heights were all referenced to the DTU21 mean sea surface to ensure a consistent reference. For each HRFM or ATL07 segment, the raw ATM heights falling within the corresponding along-track segment extent and an approximately

带格式的: 缩进: 首行缩进: 1 字符

删除了: the retrieval of surface heights and surface-type classifications

删除了: reference sea level

删除了:

删除了: establishment of an optimal

删除了: reference sea level

删除了: a

删除了:

删除了: mitigate

删除了: elevations

删除了: taken

删除了: reference sea level

删除了: where no valid lead detections are available

删除了: reference sea level

删除了:

删除了:

删除了: ATM heights within ~10 km segments are averaged within the spatial extent corresponding to HRFM and ATL07 segments, following the approach of

11 m footprint were averaged to obtain the reference ATM height. The averaged ATM heights associated with ATL07 segments are subsequently resampled to the HRFM segment spacing to facilitate a consistent comparison and to illustrate the resolution differences between the two products.

Among the four ATM underflights acquired on 8, 12, 19, and 22 April 2019, the 22 April case provides the clearest overlap with both the strong and weak ICESat-2 beams and is therefore used for the main validation shown in Fig. 7. Additional checks for the 8 and 12 April underflights are provided in Figure A3 and Figure A4, respectively. The 19 April underflight was examined but was not used for quantitative statistics because the spatial overlap with the corresponding ICESat-2 ground track was insufficient for a reliable segment-wise comparison. Because no along-track shifting was applied in this study, the reported RMSE and correlation values should be interpreted as a relative comparison between HRFM and ATL07 under the same non-shifted collocation framework, rather than as a strict replication of the optimized ATM–ICESat-2 validation procedure of Kwok et al. (2019a).

Figure 7a and **b** summarize the correlation coefficient (r) and root-mean-square error (RMSE) between ATM observations and IS-2 surface heights from HRFM and ATL07 for the strong beam (gt2l) and weak beam (gt2r) on 22 April 2019. The 25 along-track 10-km segments are ordered by mean photon rate. For both beams, HRFM shows higher correlations with ATM, with r = 0.95 ± 0.01 for the strong beam and r = 0.87 ± 0.04 for the weak beam, compared with r = 0.90 ± 0.05 and r = 0.73 ± 0.12 for ATL07, respectively. HRFM also achieves lower RMSE values of 0.08 ± 0.01 m and 0.13 ± 0.02 m, for the strong and weak beams, respectively, compared with 0.12 ± 0.03 m and 0.19 ± 0.05 m for ATL07. The improvement is most evident in segments with lower photon rates, such as segments 1-14, indicating that the HRFM photon-filtering strategy improves surface-height retrieval under low signal-to-noise conditions, particularly for the weak beam.

The along-track profiles for a representative case (segment 4) are shown in **Figure 7e** and **f** for the strong and weak beams, respectively. HRFM closely follows the ATM profile and captures height variability associated with ice ridges. In contrast, ATL07 produces smoother profiles and does not fully resolve some peak ridge heights. **Figure 7g** and **h** present the distributions of surface height estimates from HRFM, ATL07, and ATM aggregated over all 25 segments. The aggregated distributions further show that HRFM is closer to ATM in mean, median, and mode. In comparison, the ATL07 distributions are shifted towards lower heights, with mean, median, and mode values approximately 0.02–0.04 m lower than those of ATM, which is consistent with previous studies (Duncan and Farrell, 2022; Kwok et al., 2019a; Ricker et al., 2023). As indicated by the sample counts shown in parentheses, HRFM retains more valid surface-height samples than ATL07 across the examined segments. By refining the signal photon extraction and operating at a fixed 5 m along-track scale, HRFM preserves a larger fraction of observations associated with individual ridges and provides denser valid surface-height samples.

带格式的: 缩进: 首行缩进: 1 字符

删除了: **Fig. 7**…**a** and **b** summarize the correlation coefficient (r) and root-mean-square error (RMSE) between ATM observations and IS-2 surface heights (…rom HRFM and ATL07)…for the strong beam (gt2l) and weak (gt2r)…beam (gt2r)s…on 22 April 2019.,…The 25 along-track 10-km segments are ordered by mean photon rate.across the twenty-five segments ordered by mean photon rate.…The validation results of 08 April 2019 are provided in **Fig. A**3. ...

设置了格式: 字体: 小五, 加粗

删除了: consistently …igher correlations with ATM, (…ith r = 0.95 ± 0.01 for the strong beam and r = 0.87 ± 0.04 for the weak beam, compared with)…r = than ATL07 (….90 ± 0.05 and r = ….73 ± 0.12, respectively)…for ATL07, respectively. Correspondingly, …RFM also achieves lower RMSE values of 0.08 ± 0.01 m and 0.13 ± 0.02 m, for the strong and weak beams, respectively, compared with representing reductions relative to ATL07 (….12 ± 0.03 m and 0.19 ± 0.05 m for ATL07)… The improvement is most evident in segments with lower photon rates, such as(e.g.,…Segments …egments 1- to …4)… indicating that the HRFM photon-filtering strategy improves surface-height retrieval under low signal-to-noise conditions, particularly for the weak beam.It indicates the robustness of HRFM's photon extraction strategy under low signal-to-noise conditions, particularly for the weak beam. ...

删除了: **Fig. 7**…**e** and **f** for the strong and weak beams, respectively. HRFM closely follows the ATM profile and,…capturesing…the …eight variability associated with ice ridgesfine-scale height variability associated with ice ridges and surface roughness… In contrast, ATL07 produces smoother profiles and does not fully resolve some peak ridge heightsthat fail to resolve peak ridge heights and exhibits intermittent data gaps, most notably for the weak beam ...

设置了格式: 字体: 小五, 加粗

删除了: **Fig. 7…g** and **h** present the distributions of surface- …eight estimates from HRFM, ATL07, and ATM aggregated over all 25twenty-five…segments. The aggregated distributions further confirm …how that HRFM is closer to ATM in mean, median, and mode.distributions align more closely with ATM in mean, median, and mode.…In comparison, the ATL07 distributions are shifted towards lower heights, with mean, median, and mode valuessurface heights…approximately 0.02–0.04 m lower than those of ATMthat are approximately 0.02 – 0.04 m lower than those of the ATM… which is consistent with previous studies (Duncan and Farrell, 2022; Kwok et al., 2019a; Ricker et al., 2023). By refining the signal photon extraction and operating at a higher effective resolution, HRFM preserves a larger fraction of observations associated with individual ridges, resulting in a surface height distribution that better represents the observed variability.…As indicated by the sample counts shown in parentheses, HRFM retains more valid surface-height samples than ATL07twice as many valid surface samples as ATL07… ...

设置了格式: 字体: 小五, 加粗

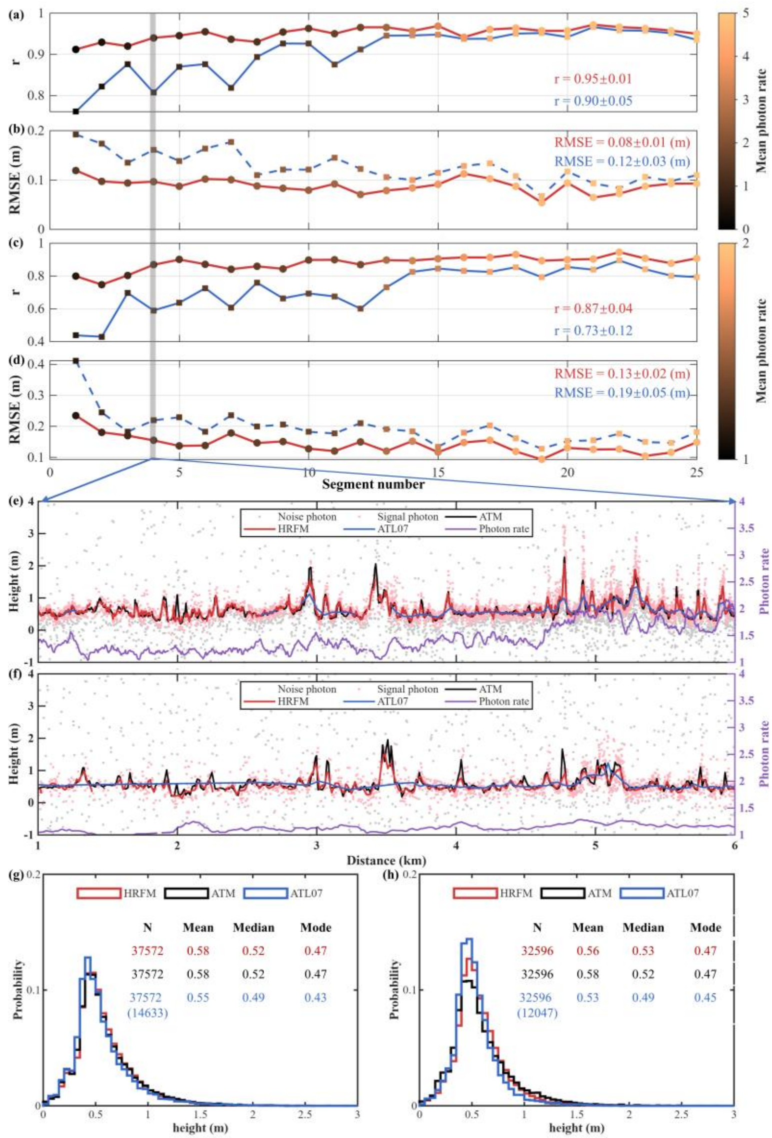

(g) N	Mean	Median	Mode
37572	0.58	0.52	0.47
37572	0.58	0.52	0.47
37572 (14633)	0.55	0.49	0.43

(h) N	Mean	Median	Mode
32596	0.56	0.53	0.47
32596	0.58	0.52	0.47
32596 (12047)	0.53	0.49	0.45

Figure 7. Evaluation of HRFM and ATL07 surface-height retrievals against ATM observations obtained on 22 April 2019. The comparison was performed using direct, non-shifted collocation, with HRFM, ATL07, and ATM heights referenced to the DTU21 mean sea surface. (a, b) Correlation coefficient (r) and root-mean-square error (RMSE) between ATM and ICESat-2 surface heights from HRFM (red) and ATL07 (blue) for the strong beam. (c, d) Same as (a, b), but for the weak beam. The color scale indicates the mean photon rate for each segment. (e, f) Surface-height profiles of segment 4 for strong and weak beams, respectively, including ATM heights (black), HRFM heights (red), ATL07 heights (blue), HRFM-identified signal (pink) and noise (gray) photons, and the corresponding photon rate (purple). (g, h) Distributions of surface-height estimate for all 25 segments for strong and weak beams, respectively, with the number of observations (N), mean, median, and mode indicated for each dataset. Numbers in parentheses denote the original number of ATL07 samples before resampling.

Table 1 summarizes the modal values of the upper 3%, 5%, and 10% of the surface-height distributions for HRFM, ATL07, and ATM for both strong and weak beams, together with their pairwise differences. The differences between HRFM and ATM modes remain small (−0.02 to +0.03 m) and show no dependence on percentile or beam type. ATL07 modes are lower than the corresponding ATM modes in all cases. This difference is particularly large for the weak beam, reaching -0.19 to -0.23 m at the 3-10% levels. These results further indicate that the stronger smoothing in ATL07 can reduce the representation of ridge-related surface-height extremes, with potential implications for estimates of sea-ice surface roughness and associated processes such as atmospheric form drag, wind stress, and ice–structure interactions (e.g., Krumpen et al., 2025; Mchedlishvili et al., 2023; Muilwijk et al., 2024).

Table 1 Modal surface-height values (m) derived from the upper 3%, 5%, and 10% of the height distributions for HRFM, ATL07, and ATM from strong and weak beams. Values in parentheses indicate the number of valid observations (N).

	Strong beam			Weak beam		
Percentile	3%	5%	10%	3%	5%	10%
HRFM_mode	1.39 (N=1102)	1.21 (N=1837)	1.02 (N=3674)	1.36 (N=837)	1.20 (N=1395)	1.01 (N=2791)
ATL07_mode	1.35 (N=439)	1.17 (N=732)	0.97 (N=1463)	1.11 (N=361)	0.97 (N=602)	0.82 (N=1205)
ATM_mode	1.37 (N=1102)	1.23 (N=1837)	1.0 (N=3674)	1.33 (N=837)	1.20 (N=1395)	1.01 (N=2791)
HRFM-ATL07	0.04	0.04	0.05	0.25	0.23	0.19
HRFM-ATM	0.02	-0.02	-0.01	0.03	0.00	0.00
ATL07-ATM	-0.02	-0.05	-0.06	-0.22	-0.23	-0.19

While the ATM comparison provides a quantitative validation of HRFM surface-height retrieval over thick, consolidated ice, the available ATM observations are mainly located north of Greenland, where the sea-ice surface is relatively rough and open-water leads are infrequent. To further assess the impact of signal photon extraction on surface-height estimation under flat-surface conditions, we examine two cases with open-water lead cases using ICESat-2 observations and coincident Sentinel-2 imagery.

Figure 8 illustrates the signal-photon extraction and surface-height retrieval over two visually identifiable open-water leads, as confirmed by the coincident Sentinel-2 imagery in Figure 8a and d. In the photon-profile panels (Fig. 8b and e), HRFM

删除了: :
删除了:
删除了: heights
删除了: (a) and (b)
删除了: HRFM (red) and ATL07 (blue) against ATM for strong beam.
删除了: (c) and (d) The same statistics for weak beams.
删除了: (e) and (f)
删除了:
删除了: (g) and (h)
删除了: The d
删除了:
删除了: Table 1
删除了: surface height distributions for HRFM, ATL07, and ATM derived from the upper 3%, 5%, and 10% of heights for both strong and weak beams,
删除了: the
删除了: In contrast,
删除了: underestimates surface height modes relative to ATM, with negative ATL07 – ATM differences observed in all cases.
删除了: This underestimation increases is markedly amplified for weak beams,
删除了: –
删除了: –
删除了: –
删除了: These results further demonstrate that smoother surface retrieval produced by ATL07 leads to an underestimation of ridge-related surface height extremes, with downstream implications for the estimations of sea ice surface roughness and associated processes ...
删除了:
删除了: unit:
删除了:
删除了: it should be noted that ATM observations are primarily ...
删除了:
删除了: derived from IS-2 observations
删除了: Fig. 8
设置了格式: 字体: 小五
设置了格式: 字体: 非加粗
删除了: a and c visualize the signal photon extractions and surfac ...
设置了格式: 字体: 非加粗
设置了格式: 字体: 加粗
设置了格式: 字体: 加粗

distinguishes between noise (gray), signal (pink), and after-pulse (orange) photons, producing relatively stable surface-height estimates (red lines) over the selected lead regions. By contrast, the ATL07 signal-selection envelope (green dashed lines) incorporates a broader range of lower-height photons in these cases, including photons associated with subsurface scattering and detector after-pulses. This leads to physically inconsistent height fluctuations in the ATL07 profile (blue lines).

Because open-water leads are expected to have relatively flat surfaces over these short distances, the downward excursions in the ATL07 profiles are more likely related to the inclusion of non-surface photons than to true surface topography. The height distributions in **Figure 8c** and **f** further illustrate this difference. HRFM produces narrow, approximately unimodal height distributions, whereas ATL07 shows broader and, in these examples, partly bimodal distributions. The lower ATL07 modes are located approximately 0.05–0.10 m below the HRFM peak, and the mean ATL07 lead heights are 0.03–0.04 m lower than the corresponding HRFM estimates.

These examples indicate that after-pulse photons can affect lead height estimation when they are identified as signal photon. If such lead segments are used to construct the local sea-surface reference, the lowered lead-height estimate would propagate into the freeboard retrieval and could lead to a positive freeboard bias of approximately 0.03–0.04 m in these cases. This highlights the importance of robust photon filtering and after-pulse treatment for high-resolution freeboard retrieval.

删除了: effectively

删除了: and therefore produces stable surface heights (red lines)

删除了: In

删除了:

删除了: significant fraction

删除了: of subsurface scattering and after-pulse photons.

删除了: Given that open-water leads should exhibit a flat surface, the downward spikes and increased variability in ATL07 are results of poor signal-noise separation related to after-pulse photons rather than true topographic features.

删除了: **(Fig. 8b**

删除了: **d**

删除了:)

删除了: quantify this discrepancy.

设置了格式: 字体: 小五, 加粗

删除了: While HRFM yields unimodal distributions with well-defined peaks, ATL07 exhibits bimodal distributions.

删除了: The primary ATL07 mode is shifted downward by approximately 0.05 – 0.10 m due to the inclusion of after-pulse photons. Consequently, the mean ATL07 height is 0.03 – 0.04 m lower than the HRFM estimate.

删除了: Crucially, these low-value signals do not represent the physical water surface; rather, they would introduce a negative bias in reference sea level estimates. If uncorrected, this systematic underestimation of lead heights would lead to an overestimation of sea ice freeboard by ~0.03 – 0.04 m, ultimately propagating errors into the calculation of sea ice thickness.

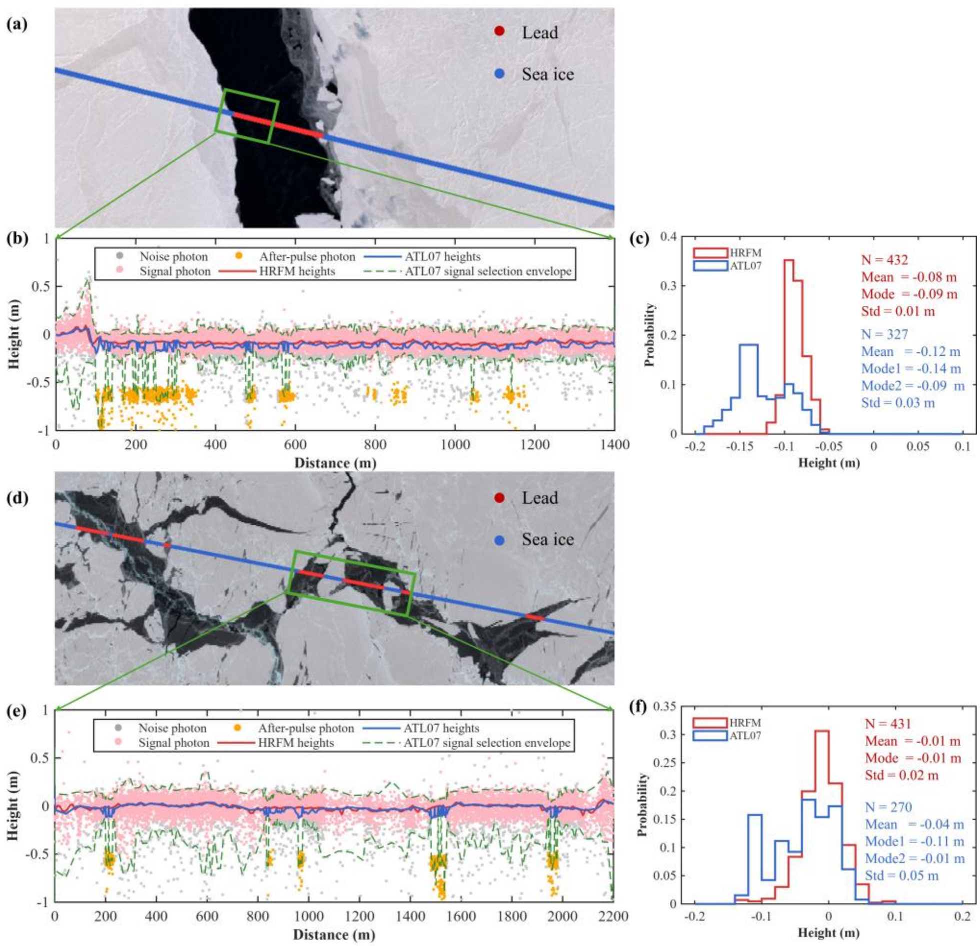

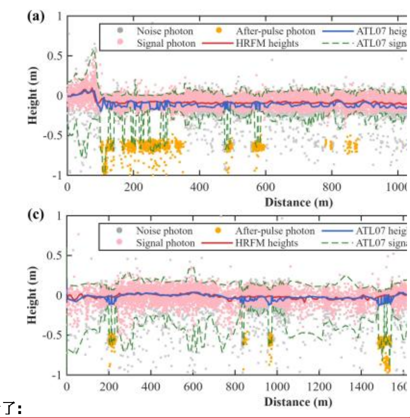

删除了:

Figure 8. Surface-height retrieval over open-water leads and comparison between HRFM and ATL07 for ATL03_20220424135203_04961504_006 and ATL03_20220510145813_07411505_006. (a, d) Coincident Sentinel-2 imagery showing the ICESat-2 ground tracks and HRFM surface-type classification. Red and blue points indicate lead and sea-ice segments, respectively, and the green boxes mark the enlarged regions shown in the photon-profile panels. (b, e) Along-track ATL03 photon clouds and surface-height retrievals within the selected lead regions. Gray, pink, and orange points denote background, signal, and after-pulse photons identified by HRFM, respectively. The green dashed lines represent the ATL07 signal-selection envelope. The

删除了: :

red lines show HRFM surface heights, while the blue lines represent ATL07 surface heights. (c, f) Probability distributions of surface-height estimates derived from HRFM (red) and ATL07 (blue) within the selected lead regions.

4.2 Surface-type classification validation and comparison

Figure 9 provides a qualitative validation of HRFM surface-type classification using coincident Sentinel-2 imagery as an independent visual reference, together with a direct comparison against ATL07 across a range of observation conditions. For ATL07, two surface-type flags are considered: *height_segment_type* and *ssh_flag*, as described in **Sect. 2.1.2**.

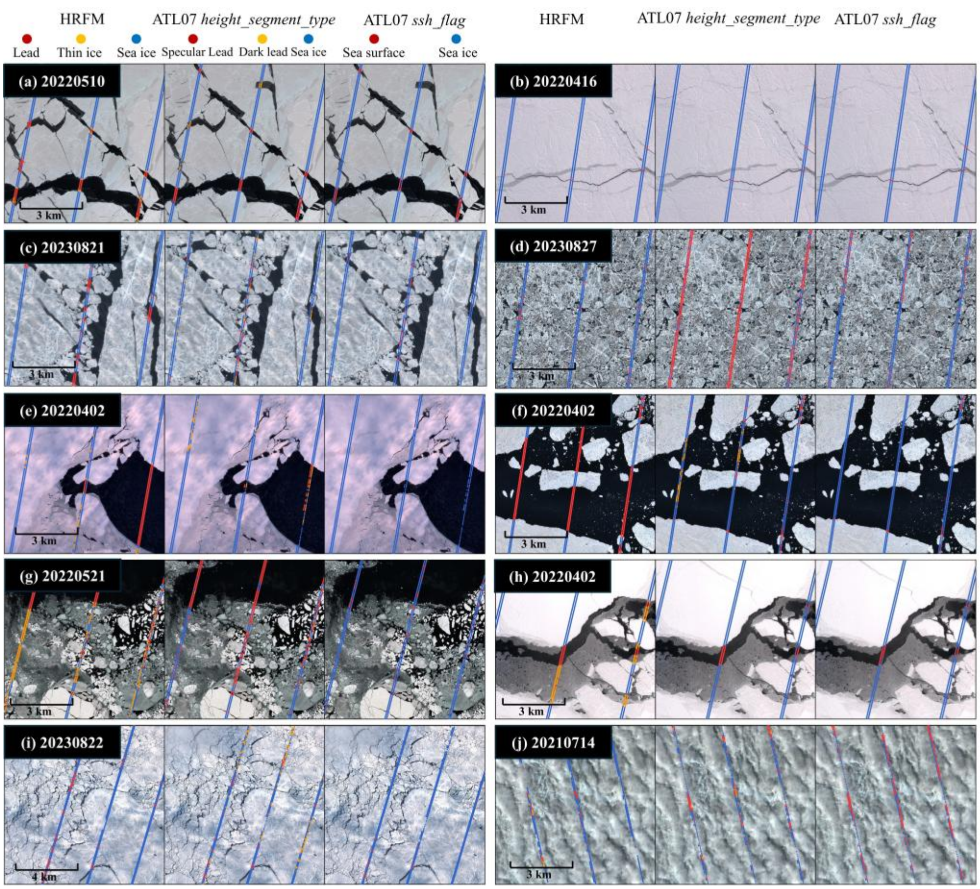

删除了: Surface height retrieval over open-water leads and comparison between HRFM and ATL07 for ATL03_20220424135203_04961504_006 and ATL03_20220510145813_07411505_006. (a, c) Along-track photon clouds and surface height retrievals for two open-water lead regions. Gray, pink and orange points denote noise, signal ...

删除了:

删除了: Figure 9

删除了: to

删除了: (

删除了:)

设置了格式: 字体: 非倾斜

设置了格式: 字体: 加粗

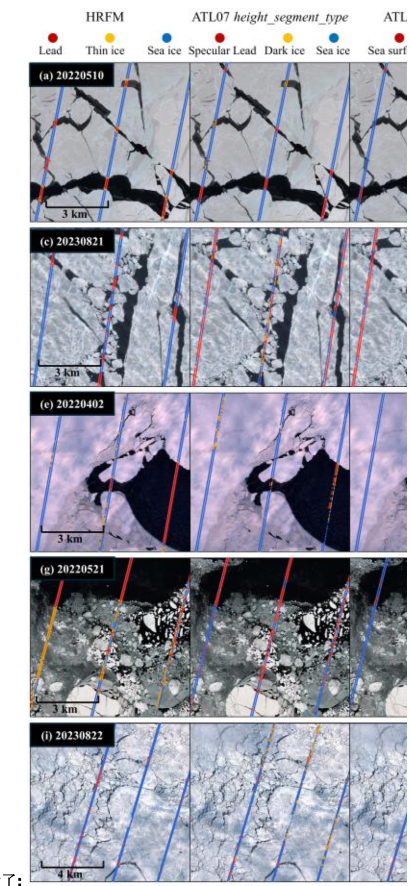

删除了:

Figure 9: Comparison of surface-type classification from HRFM and ATL07 for (a, b) winter cases, (c, d) summer melt-season cases, (e, f) large-lead cases, (g-h) thin-ice cases, (i, j) cloud-affected cases. Coincident Sentinel-2 optical images acquired within 30 min of the ICESat-2 tracks are used as the independent visual reference for evaluating the classifications. The HRFM classification results are from Leave-One-Group-Out (LOGO) tests. Background images are coincident Sentinel-2 optical images acquired within 30 minutes of the ICESat-2 tracks. The ICESat-2 footprint size is not to scale.

Under favorable winter conditions (**Figure 9a** and **b**), the HRFM and ATL07 classifications are generally consistent with the Sentinel-2 imagery for both strong and weak beams. Both methods detect major leads at the kilometer scale and narrow cracks smaller than approximately 50 m. The agreement between strong and weak beams in these cases indicates that classification is less limited by beam energy under high-contrast winter surface conditions.

The differences between HRFM and ATL07 become more evident under challenging surface conditions. During the summer melt season (**Figure 9c** and **d**), widespread melt ponds increase photon rates (**Figure 5b**) and photon densities (**Figure 5c**), reducing the contrast between open water and melt-pond-covered ice. The fixed-threshold algorithm used in ATL07, originally tuned for winter conditions, associates high photon rates with open water and therefore misclassifies segments of melt-pond-covered ice as leads. If such segments are used in local sea-surface reference construction, elevated ice or melt-pond surface heights may be included in the reference surface, which can introduce a negative bias in the retrieved freeboard. In these cases, HRFM more consistently distinguishes true open-water leads from melt-pond-covered ice, producing surface-type classifications that agree more closely with Sentinel-2 imagery.

Figure 9e and **f** illustrate additional differences related to large dark leads. Large leads with low albedo and wind-roughened surfaces often exhibit reduced specular returns and lower photon rates and photon densities (**Figure 5**). Under these conditions, ATL07 may classify portions of open water as dark leads or sea ice. As dark-lead segments are not used as sea-surface segments in ATL07, their exclusion reduces the number of valid open-water samples available for local sea-surface reference estimation. This can increase the uncertainty of the reference sea level and subsequently affect freeboard retrieval. In contrast, HRFM identifies these visually apparent open-water regions as leads more consistently, particularly where specular returns are sparse.

Beyond lead detection, **Figure 9g** and **h** show that HRFM can distinguish thin ice as a separate surface class in winter cases. ATL07 separates open water into specular and dark lead categories, but it does not explicitly distinguish thin ice from thicker snow-covered sea ice; most thin-ice surfaces are therefore included in the general sea-ice category. HRFM provides a finer partitioning of surface types by separating thin ice from both open water and thicker sea ice. This distinction is useful for surface-type interpretation and process studies, because thin ice is associated with enhanced conductive heat flux through the ice and stronger turbulent exchange above the surface compared with thicker ice (Uhlíková et al., 2024). However, for the final freeboard retrieval, thin ice is conservatively merged with sea ice in the binary classifier, as described below, to avoid using uncertain thin-ice segments as lead segments.

Finally, **Figure 9i** and **j** illustrate the impact of cloud-affected conditions on surface-type classification. Under optically thin clouds (**Figure 9i**), ATL07 occasionally misclassifies portions of sea ice as dark leads, as reported by Kwok et al. (2021). Under optically thick clouds (Figure 9**j**), cloud scattering can weaken the effective surface return, reduce photon rates, and distort classification features, leading to missing observations or misclassification in both HRFM and ATL07. To reduce the influence

删除了: **…ype classification from HRFM and ATL07 in …or (a, b) winter cases, (c, d) summer melt-season cases, (e, f) large-lead cases, (g-h) gray…hin-ice cases, (i, j) cloud -affected-cover** ...

删除了: **Fig. 9**…**a** and **b**), the HRFM and ATL07 classifications are generally consistent with the Sentinel-2 imagery for both strong and weak beams. Both methods detect major leads and narrow cracks smaller than approximately 50 m.(~1 km scale) and narrow cracks (< 50 m),…The agreement between strong and weak beams in these cases indicates that classification is less limited by beam energy under high-contrast winter surface conditions.and there are no apparent differences between beam types. This indicates that classification is not limited by beam energy. ...

设置了格式: 字体: 小五, 加粗

删除了: In contrast, t

删除了: **Fig. 9**

删除了: **Fig. 5**

删除了: **Fig. 5**…**c**), reducing the contrast between open water and melt-pond-covered ice. The fixed-threshold algorithm used in ATL07, originally tuned for winter conditions, associates high photon rates with open water and therefore misclassifies segments of melt-pond-covered ice as leads. If such segments are used in local sea-surface reference construction, elevated ice or melt-pond surface heights may be included in the reference surface, which can introduce a negative bias in the retrieved freeboard.This could result in some sea ice heights being included in the reference sea level, which would lead to a low bias in freeboard estimates.…In these cases, HRFM consistently distinguishes true open-water leads from melt-pond-covered ice, producing surface-type labels ...

设置了格式: 字体: 小五, 加粗

设置了格式: 字体: 小五, 加粗

设置了格式: 字体: 小五, 加粗

删除了: **Fig. 9**…**e** and **f** illustrate additional differences related to large dark leads.limitations of ATL07 related to dark leads. ...

设置了格式: 字体: 小五, 加粗

删除了: **Fig. 5**…).,…Under these conditions, ATL07 may classify portions of open water as dark leads or sea ice.leading ATL07 to label portions of open water as dark leads or sea ice.…As dark-lead segments are not used as sea-surface segmentsare excluded from the reference sea level…in ATL07, their exclusionomission…reduces the number of valid open-water samples available for local sea-surface reference estimation.sea surface height determination.…This there ...

设置了格式: 字体: 小五, 加粗

删除了: **Fig. 9**…**g** and **h** show that HRFM can distinguish thin ice as a separate surface class in winter cases.demonstrate HRFM's abilit ...

设置了格式: 字体: 小五, 加粗

删除了: **Fig. 9**…**i** and **j** illustrate the impact of cloud-affectedclou ...

设置了格式: 字体: 小五, 加粗

删除了: **Fig. 9**

设置了格式: 字体: 小五, 加粗

删除了: **Fig. 9**…**j**), cloud scattering can weaken the effective surface return, reduce photon rates, and distort classification features, lead ...

of such cases in subsequent freeboard retrieval, HRFM lead segments with fewer than 10 valid signal photons and a height standard deviation greater than 0.8 m are excluded from local sea-surface reference construction.

Table 2 summarizes the LOGO cross-validation results for the HRFM three-class surface-type classifier. Statistics are reported separately for strong and weak beams, including overall accuracy, precision, and recall values. Here, precision value quantifies false positives, defined as the fraction of correctly classified segments among all segments assigned to a class, whereas recall value quantifies false negatives, defined as the fraction of correctly classified segments among all reference segments of that class.

For both beam types, HRFM achieves high overall accuracy, with 0.98 for strong beams and 0.97 for weak beams. For strong beams, sea ice is classified with a precision of 0.99 and a recall of 0.99, while lead detection reaches a precision of 0.96 and a recall of 0.95. For weak beams, sea ice classification, with a precision of 0.98 and a recall of 0.99, whereas lead performance is slightly reduced, with a precision of 0.94 and a recall of 0.91. This reduction is consistent with weaker photon statistics and lower signal-to-noise ratios that can blur the separation between open water and low-reflectance ice surfaces.

Table 2 Confusion matrices and classification accuracy statistics for the HRFM three-class surface-type classifier based on leave-one-group-out (LOGO) cross-validation over tracks with a total length of approximately 10,000 km.

Strong beam		Ground truth from Sentinel-2				Precision
		Sea ice	Lead	Thin ice	All	
HRFM surface type	Sea ice	902,888	1,787	10,056	914,731	0.99
	Lead	166	90,149	3,665	93,980	0.96
	Thin ice	3,464	3,194	13,920	20,578	0.67
	All	906,518	95,130	27,641	1,029,289	
Recall		0.99	0.95	0.50		0.98

Weak beam		Ground truth from Sentinel-2				Precision
		Sea ice	Lead	Thin ice	All	
HRFM surface type	Sea ice	904,947	3,410	12,341	920,698	0.98
	Lead	730	78,172	4,509	83,411	0.94
	Thin ice	3,224	3,970	12,592	19,786	0.64
	All	908,901	85,552	29,442	1,023,895	
Recall		0.99	0.91	0.43		0.97

Classification uncertainty is larger for thin ice. The precision and recall for thin ice are 0.67 and 0.50 for strong beams and decrease to 0.64 and 0.43 for weak beams. This is expected because thin ice represents a transitional surface state: its photon rate, background rate, height standard deviation and photon density often fall between those of snow-covered ice and leads, leading to overlapping feature distributions and increased confusion. In addition, thin-ice labeling from Sentinel-2 imagery is

删除了: To mitigate this effect in subsequent freeboard retrieval, HRFM lead segments with fewer than 10 valid signal photons and a height standard deviation exceeding 0.8 m are excluded.
删除了: **Table** 2
删除了: classification
删除了: obtained
删除了: 0.99 precision and 0.99 recall
删除了: leads reach 0.96 precision and 0.95 recall.
删除了:
删除了: remains robust (0.98 precision and 0.99 recall)
删除了: whereas lead performance is slightly reduced (0.94 precision and 0.91 recall),
删除了: **the**
删除了: ~
删除了: P
删除了: gray
删除了: gray

intrinsically less certain than the identification of open water or bright snow-covered ice which propagates into the reference labels and limits achievable class separability.

To isolate the classification performance most directly affecting freeboard retrieval, we also evaluated a two-class setting in which thin ice is merged into sea ice class. Overall accuracy increases to 0.99 for strong beams and 0.99 for weak beams (Table A1), indicating that most errors in the three-class problem arise from ambiguity within ice subclasses rather than from confusion between sea ice and leads. Therefore, the final full-year HRFM freeboard retrieval uses the binary RF classifier with only two classes, sea ice and lead. This conservative setting reduces the risk of using uncertain thin-ice segments as lead segments for local sea-surface reference estimation.

After this independent evaluation, the final binary RF classifier was trained using all 25 labelled scenes and applied to the full-year HRFM data.

删除了: identifying

删除了: ,

删除了:

删除了: Table A1

域代码已更改

删除了: Overall, HRFM produces consistent surface-type labels along both strong and weak beams across a range of conditions, supporting reliable identification of lead segments that define the local reference sea level used for freeboard estimation.

4.3 Year-round sea-ice freeboard

删除了:

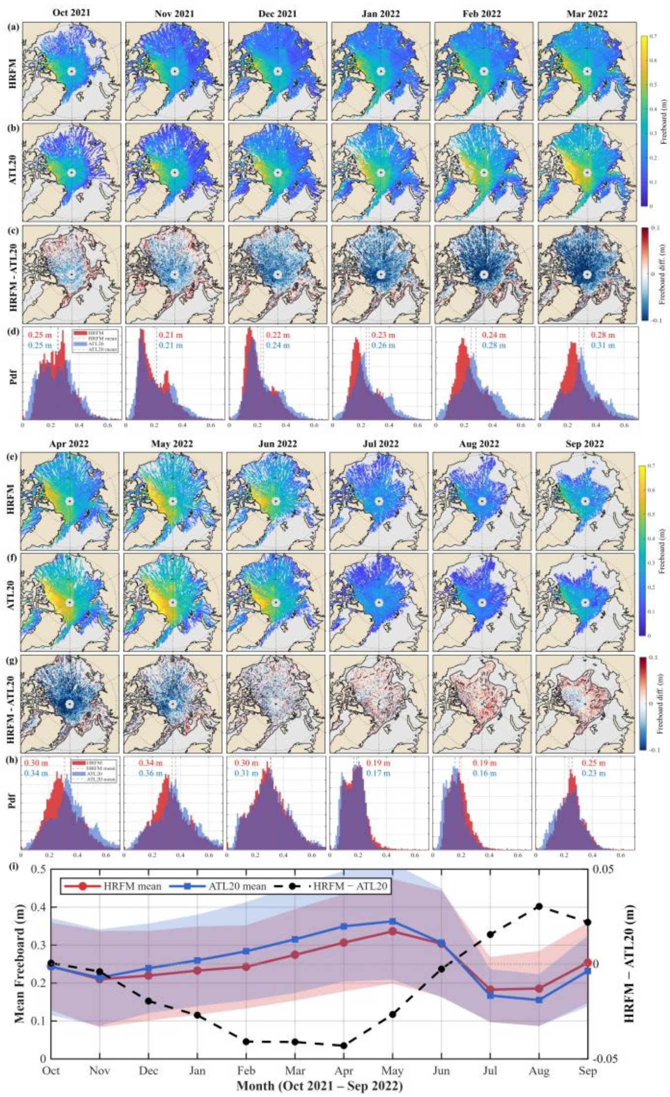

Figure 10: Monthly gridded sea-ice freeboard from October 2021 to September 2022. (a, e) Monthly mean freeboard estimated using HRFM. (b, f) Corresponding monthly mean freeboard from the ATL20 product. (c, g) Spatial differences between the two products (HRFM – ATL20). (d, h) Histograms of gridded freeboard for HRFM (red) and ATL20 (blue), with dashed vertical lines indicating the respective monthly means. (i) Time series of monthly mean freeboards from HRFM (red) and ATL20 (blue), with shaded areas representing ±1 standard deviation around the monthly mean. The dashed black line indicates the monthly mean difference between HRFM and ATL20.

The gridded freeboard estimates from HRFM and the official ATL20 product from October 2021 to September 2022 are compared in **Figure 10**. The within-grid-cell standard deviations of the monthly HRFM freeboards are shown in Figure A6. To facilitate comparison with ATL20, which is generated from strong-beam ATL10 freeboards, this gridded comparison uses HRFM retrievals from the central strong beam. During this one-year demonstration period, HRFM provides monthly freeboard estimates over most of the Arctic Ocean and shows broader spatial coverage than ATL20 in several months. Both products display broadly consistent Arctic-wide spatial distribution patterns (**Figure 10a–b, e–f**), with larger freeboards generally found north of Greenland and the Canadian Arctic Archipelago. These regions are associated with older sea ice and thicker snow cover. The histograms of gridded freeboard (**Figure 10d** and **h**) further illustrate the statistical consistency between the two products.

The spatial distribution of freeboard differences (HRFM − ATL20) reveals two distinct patterns related to zones of SIC (**Figure 10c** and **g**). Positive differences are mainly observed in low-SIC regions (<90%), whereas negative differences dominate in high-SIC areas (>90%). large and dynamically evolving leads are more frequent, and the local sea-surface reference can be difficult to estimate robustly. Ocean–ice interactions, waves, and swell within expansive leads may introduce additional height variability (Bateson et al., 2020), so a limited set of detected lead samples may not fully represent the local sea-surface height. In this context, gridded freeboard differences between HRFM and ATL20 may partly reflect the different lead-detection strategies used in the two products. HRFM identifies a larger population of visually apparent lead segments, whereas the ATL07 processing chain uses a more conservative set of sea-surface segments. Conversely, in compact high-SIC areas dominated by thick ice, leads are sparse. As noted by Petty et al. (2021), there are fewer specular leads available from the ATL07 product in these regions compared to more seasonal ice regions, which can lead to the freeboard difference between the ATL07-based ATL20 product and our HRFM.

The monthly evolution of basin-averaged freeboard during this one-year demonstration period is shown in **Figure 10i**. HRFM yields lower mean freeboard than ATL20 from October to May, whereas it yields slightly higher mean freeboard during much of the melt season from June to September. These monthly differences likely arise from the combined effects of factors related to surface-height retrieval, lead detection, local sea-level reference construction, and gridding. During winter, narrow and smooth leads are more susceptible to ATLAS detector saturation, which can generate after-pulse photons below the true water surface (**Figure 8**). HRFM explicitly identifies and removes such after-pulse returns, whereas residual noise photons may still be included in the ATL07 signal-selection envelope in some cases. This can lower the estimated lead height and consequently increase ATL20 freeboard when such leads are used for sea-surface reference construction. In addition, the more conservative ATL07 sea-surface flag identifies a smaller subset of available leads, whereas HRFM detects a larger number of lead segments. This difference may affect the representativeness of the local sea-surface reference.

删除了: laser…freeboard estimated using the proposed… …RFM method… (b, f) Corresponding monthly mean freeboard from the ATL20 product. (c, g) Spatial differences between the two products (HRFM − … ATL20). (d, h) Histograms of gridded freeboard for HRFM (red) and ATL20 (blue), with dashed vertical lines indicating the respective monthly means. (i) Time series of monthly mean freeboards from HRFM (red) and ATL20 (blue), with shaded areas representing ±1 standard deviation around the monthly mean.,…The dashed black line indicates the monthly mean difference between HRFM and ATL20.and the corresponding mean difference (HRFM − ATL20, dashed black line).

删除了: Fig. 10…. The within-grid-cell standard deviations of the monthly HRFM freeboards areStandard deviation of freeboards in each monthly grid cell is…shown in

删除了: Fig. A5

设置了格式: 字体: 小五, 加粗

删除了: Utilizing data from the central strong beam, HRFM provides year-round freeboard estimates over most of the Arctic Ocean, with broader spatial coverage than ATL20 in several months.…During this one-year demonstration period, HRFM provides monthly freeboard estimates over most of the Arctic Ocean and shows broader spatial coverage than ATL20 in several months. Both products display broadlyhighly

删除了: Fig. 10…**a–b, e–f**), with larger freeboards generally found north of Greenland and the Canadian Arctic Archipelago.characterized by increasing freeboard from the central Arctic toward the marginal seas and persistently high values north of Greenland and the Canadian Arctic Archipelago,…These regions are associated withclosely associated with… the presence of …lder sea ice and thicker snow cover in these areas

设置了格式: 字体: 加粗

删除了: Fig. 10

设置了格式: 字体: 小五, 加粗

删除了: Fig. 10…**c** and **g**). Positive differences are mainly observed in low-SIC regions (<90%), whereas negative differences dominate in high-SIC areas (>90%). large and dynamically evolving leads are more frequent, and the local sea-surface reference can be difficult to estimate robustly. Ocean–ice interactions, waves, and swell within expansive leads may introduce additional height variability In the

设置了格式: 字体: 小五, 加粗

删除了: within expansive leads, the limited sampling of lead heights may fail to capture a statistically representative reference sea level, leading to substantial estimation uncertainties.…In this context,

删除了: seasonal…onthly …volution of basin-averaged freeboard during this one-year demonstration period is shown in (

删除了: Fig. 10…**i.**)…f…RFM yields lower mean freeboard than ATL20 from October to May, whereas it yields slightly higher mean freeboard during much of the melt season from June to

设置了格式: 字体: 小五, 加粗

删除了: Fig. 8…). HRFM explicitly identifies and removes such after-pulse returns, whereas residual noise photons may still be included inremain in…the ATL07 signal-selection envelope in som

设置了格式: 字体: 小五, 加粗

During the melt season, melt-pond-covered ice becomes more prevalent, increasing the likelihood that pond-covered ice surfaces are confused with open-water leads in threshold-based classification (**Figure 9c, d**). If such segments are used as sea-surface reference points, the reference surface may be biased upward, leading to lower freeboard estimates. HRFM reduces this risk by using a machine-learning classifier trained with Sentinel-2-assisted labels and by conservatively excluding melt-pond-affected segments from lead-based sea-surface reference construction. These differences in lead identification and surface-height filtering provide a plausible explanation for the monthly HRFM–ATL20 differences observed during the one-year demonstration period. The combined effects of improved surface-height retrieval and surface-type classification on along-track freeboard estimation are further examined in Sect. 5.2.

Although HRFM demonstrates improved performance in along-track surface-height retrieval and surface-type classification relative to ATL07, systematic differences remain between gridded HRFM freeboards and the ATL20 product. It should be noted that differences in reference sea-level construction and gridding methods may also contribute to the observed discrepancies at the grid scale. The observed differences provide a valuable insight into how surface-height retrieval and lead detection strategies influence basin-scale freeboard estimates.

5 Discussion

5.1 Inter-beam consistency and weak-beam performance

IS-2 uses a multibeam configuration consisting of three strong-weak beam pairs. The weak beams transmit approximately 25% of the energy of the strong beams and have therefore been used less extensively in sea-ice studies because of their lower signal-to-noise ratios. One objective of this study is to evaluate whether HRFM can provide stable freeboard retrievals from weak-beam observations and thereby increase effective sampling density and spatial coverage. In addition, previous studies have reported inter-beam range biases in IS-2 observations, including centimeter-level differences among strong beams in Arctic sea-surface height anomaly retrievals (Bagnardi et al., 2021) and ice-sheet elevation measurements (Brunt et al., 2021), with persistent biases associated with strong beam 1. Such inter-beam inconsistencies raise concerns about the joint use of six beams for freeboard estimation.

To evaluate inter-beam consistency and weak-beam performance in freeboard retrieval, we calculated the monthly mean freeboards using six different beams respectively (**Figure 11**). The monthly mean freeboards derived from the six beams show generally consistent temporal variations throughout the one-year demonstration period. During the freezing season from October to May, differences among the six beams are mostly below 0.01 m (**Figure 11a**). During the summer melt months, however, slightly larger inter-beam differences appear, particularly between the middle beam pair and the outer beam pairs. The maximum monthly deviation reaches approximately 0.02 m. This difference may be related to the increased complexity of surface conditions, lower transmitted energy level (~80% of outer beams, Kwok et al., 2019b) and decreased valid observations due to clouds compared to winter.

删除了: ATL07 misclassifies such surfaces as open-water leads
删除了: Fig. 9
设置了格式: 字体: 加粗
删除了: This misclassification may bias the reference sea surface upward and reduce the derived freeboard therefore potentially leading to an underestimation of sea ice thickness or sea ice melt during summer. In contrast, HRFM more consistently separates true open-water leads from pond-covered ice through its machine-learning surface-type classifier.
删除了: It can therefore be expected to help improve the accuracy of estimates of summer sea ice melt rates using the data derived by the HRFM (Wang et al., 2025).
删除了: utilizes
删除了: The weak beams—transmitting approximately 25% of the energy of the strong beams—have been underutilized in sea ice studies due to their lower signal-to-noise ratio (SNR).
删除了: A
删除了: primary
删除了: the proposed High-Resolution Fitting Method (
删除了:)
删除了: e
删除了: nhance freeboard retrieval under low-SNR conditions and enable weak beams to achieve performance comparable to that of strong beams, thereby increasing effective sampling density and spatial coverage.
删除了:
删除了: Fig. 11
删除了: each of
删除了: reveals
设置了格式: 字体: 小五, 加粗
删除了: high inter-beam consistency throughout the year, particularly during the freezing months (October to May),
删除了: where the differences among all six beams remain below 0.01 m
删除了:
删除了: Fig. 11
设置了格式: 字体: 小五, 加粗
删除了: a slight deviation is observed between strong beams and weak beams. …
删除了: The middle beams (Strong beam 2 and weak beam 2) exhibit a maximum deviation of approximately 0.02 m compared to the outer beams,
删除了: which may be attributed to
删除了: (
删除了:)

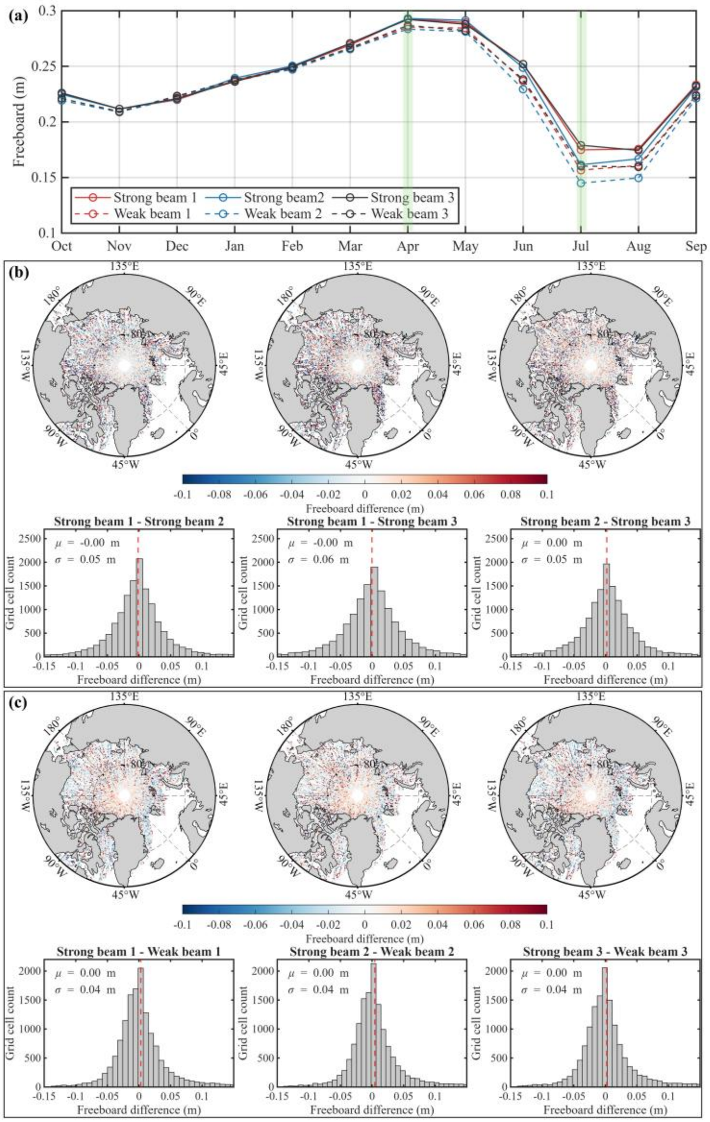
(a)
Freeboard (m)
0.3
0.25
0.2
0.15
0.1
Oct
Nov
Dec
Jan
Feb
Mar
Apr
May
Jun
Jul
Aug
Sep
Strong beam 1
Weak beam 1
Strong beam2
Weak beam 2
Strong beam 3
Weak beam 3
(b)
135°E
180°
90°E
80°
135°W
45°E
90°W
0°
45°W
-0.1 -0.08 -0.06 -0.04 -0.02 0 0.02 0.04 0.06 0.08 0.1
Freeboard difference (m)
Strong beam 1 - Strong beam 2
μ = -0.00 m
σ = 0.05 m
Strong beam 1 - Strong beam 3
μ = -0.00 m
σ = 0.06 m
Strong beam 2 - Strong beam 3
μ = 0.00 m
σ = 0.05 m
Grid cell count
Freeboard difference (m)
(c)
Strong beam 1 - Weak beam 1
μ = 0.00 m
σ = 0.04 m
Strong beam 2 - Weak beam 2
μ = 0.00 m
σ = 0.04 m
Strong beam 3 - Weak beam 3
μ = 0.00 m
σ = 0.04 m

Figure 11. Inter-beam comparison of HRFM freeboard retrievals. (a) Monthly mean freeboard from October 2021 to September 2022 for the three strong beams (solid lines) and the corresponding weak beams (dashed lines). The green vertical bands highlight April and July, which are used for the spatial inter-beam comparisons. (b) Spatial distribution of gridded freeboard differences among strong beams for April 2020 (Strong beam 1 − Strong beam 2, Strong beam 1 − Strong beam 3, and Strong beam 2 − Strong beam 3). The corresponding histograms show the mean (μ) and standard deviation (σ) of each difference distribution. (c) Same as (b), but for differences between corresponding strong–weak beam pairs (Strong beam 1 − Weak beam 1, Strong beam 2 − Weak beam 2, and Strong beam 3 − Weak beam 3).

Figure 11b and Figure A7**a** show the spatial distributions and histograms of freeboard differences among the three strong beams for April and July 2022, respectively. **Figure 11c** and Figure A7**b** show the corresponding differences between each strong–weak beam pair. In April, the differences among strong beams and between corresponding strong–weak beam pairs show no clear regional pattern across the Arctic basin. Their histograms are centered near zero, with mean differences close to 0.00 m and standard deviations of approximately 0.04–0.06 m. In July, the differences remain broadly centered near zero but show slightly larger beam-dependent offsets. In particular, the middle beam shows a mean offset of approximately −0.01 to −0.02 m relative to the outer beams, and weak beams show a small negative offset relative to their corresponding strong beams.

The limited impact of inter-beam range bias on HRFM freeboard estimates is likely related to the differential nature of freeboard retrieval. Freeboard is derived as the relative height between the ice surface and a locally determined sea-surface reference along the same beam. Therefore, beam-dependent absolute range offsets can be partly cancelled when both ice-surface heights and lead-based sea-surface references are retrieved within the same beam. By stabilizing surface-height retrieval and lead identification under low-photon conditions, HRFM further reduces the sensitivity of weak-beam retrievals to their lower transmitted energy. As a result, weak-beam freeboards are broadly consistent with strong-beam freeboards at the monthly gridded scale, although small centimetre-level inter-beam differences remain, especially during the melt season.

These results indicate that weak-beam observations can provide useful additional information for HRFM freeboard retrieval. Weak-beam freeboards not only achieve accuracy comparable to strong beams but also generate spatially coherent freeboard maps independently. This enhanced inter-beam consistency implies that future IS-2 sea ice freeboard and thickness products could benefit from jointly exploiting all six ATLAS beams. In the present HRFM framework, this means combining freeboard estimates that are independently retrieved for each beam, thereby increasing effective sampling density, improving spatial coverage, and reducing gridded uncertainty, particularly in regions and seasons where observations are otherwise sparse (Ricker et al., 2023). A related but distinct approach is to construct a swath-like sea-surface reference to retrieve sea-ice freeboard by using sea-surface points across beams, which has also been explored in ATL07/ATL10 algorithm development(Kwok et al., 2026).

5.2 Potential sources of freeboard difference

The monthly contrasting freeboard differences between HRFM and ATL20 may partly arise from differences in surface-height estimation, surface-type classification, and local sea-surface reference construction. Two examples (from winter and summer conditions) in **Figure 12** present how to determine the local sea level reference using the surface height and surface type from HRFM and ATL07 (including *height_segment_type* and *ssh_flag*). The reference sea level is the mean height of lead segments

删除了: :
删除了: **Beam comparison.**
删除了: **Shaded vertical bands**
删除了: **the representative spring (April) and summer (July) periods discussed in the text**
删除了: **,**
删除了: **together with histograms. The mean (μ) and standard deviation (σ) of each distribution are indicated.**
删除了: We show the spatial distributions and histograms of intercomparisons among the three strong beams (
删除了: **Fig. 11**
删除了: **Fig. A6**
设置了格式: 字体: 加粗
删除了:) and differences between corresponding strong-weak beam pairs (
删除了: **Fig. 11**
删除了: **Fig. A6**
设置了格式: 字体: 加粗
删除了:) for April 2022 and July 2022 (Green bar in **Fig. 11a**).
删除了: The
删除了: among the three strong beams and the three strong-weak beam pairs show no evident regional patterns across the Arctic basin.
删除了: The histograms for April 2022 show that the differences ...
删除了: It is notable that the standard deviations on the difference ...
删除了: The histograms for July 2022 show that a mean offset of ...
删除了: our
删除了: ,
删除了: which
删除了: largely cancels beam-dependent absolute range offsets
删除了:
删除了: sensitivity to energy discrepancies between strong and we ...
删除了: allowing weak beams to achieve freeboard estimates that ...
删除了: demonstrate
删除了: HRFM elevates weak beams from an auxiliary role to full ...
删除了: ,
删除了: increasing effective sampling density, improving spatial ...
删除了: seasonally
删除了: primarily originate from
删除了: the construction of the reference sea level.
删除了: **Fig. 12**
删除了: reference
设置了格式: 字体: 加粗

for HRFM, specular lead segments for ATL07 *height_segment_type* and sea surface segments for ATL07 *ssh_flag*. Above the reference level (blue line) is the freeboard of the floating ice cover.

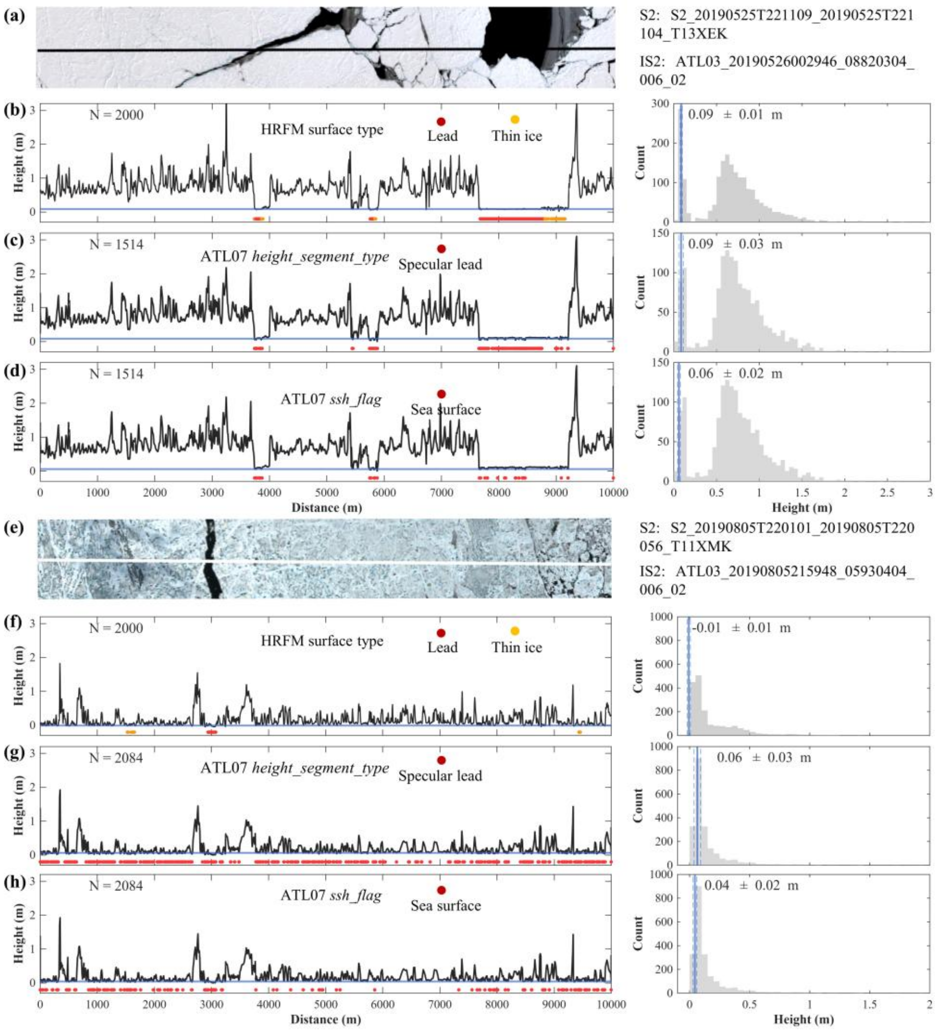

Figure 12. Determination of the local sea-surface reference in 10-km segments using surface heights and surface-type classifications from HRFM and ATL07. Two examples are shown for (a–d) 26 May 2019 and (e–h) 5 August 2019. (a, e) Coincident sentinel-2 imagery with IS-2 tracks shown in black and white. Surface heights and surface-type classifications from (b,f) HRFM, (c, g) ATL07 *height_segment_type*, and (d, h) ATL07 *ssh_flag* are used to estimate the local sea-surface references (blue lines), respectively. N is the number of height segments within each 10-km example. Quantity on right panel shows the calculated local sea-surface reference (mean and standard deviation).

For the winter example, HRFM provides surface-type classifications that are more consistent with Sentinel-2 imagery than those from ATL07, together with a more stable surface-height retrieval over lead regions (Figure 12**b**). As shown by the height distributions on the right-hand side of Figure 12, the HRFM-derived reference sea level is 0.09 ± 0.01 m, indicating that the retained lead segments form a compact and internally consistent sea-surface sample. When the ATL07 *height_segment_type* classification is used, the reference sea level is close to 0.09 m, but exhibits a larger standard deviation (0.03 m). This larger standard deviation reflects the inclusion of lead segments whose surface heights are locally underestimated, partly due to residual after-pulse photons that are not fully removed in the ATL07 processing chain, as illustrated in Figure 8. The ATL07 *ssh_flag* represents an additional height-based filtering applied to the *height_segment_type* surface types (Sect. 2.1.2). This filtering preferentially retains lower-height specular lead segments, while discarding a large fraction of valid lead segments (Figure 12**c** and **d**). Consequently, the number of retained sea-surface samples is markedly reduced, and the resulting reference sea level decreases to 0.06 ± 0.02 m, which is lower than both the HRFM- and *height_segment_type* - based estimates. This downward shift in the reference sea level explains why ATL07-based freeboard estimates (ATL20) tend to be higher than HRFM during winter conditions.

Under summer melt conditions, the dominant source of differences shifts from height filtering to surface-type misclassification. Extensive melt ponds reduce the contrast of classification features and cause ATL07 *height_segment_type* to misclassify large fractions of melt-pond-affected sea ice as leads (Figure 12**g**). Consequently, the reference sea level derived from *height_segment_type* is elevated to 0.06 ± 0.03 m, compared to the HRFM reference sea level of about -0.01 ± 0.01 m. Although the *ssh_flag* filtering removes some high-height segments and lowers the reference sea level to 0.04 ± 0.02 m (Figure 12**h**), a number of misclassified sea ice segments remain. These residual errors continue to bias the ATL07-based reference sea level upward relative to HRFM, leading to systematically lower freeboard estimates in summer.

The plots in Figure 13 best show the difference of reference sea level determination between HRFM and ATL07 during winter and summer examples. Figure 13**a** and **b** show the relevant statistics from fifty 10-km segments in the May 26, 2019 and August 05, 2019 tracks, respectively. HRFM estimates are generally higher than ATL07 in winter but lower in summer. Crucially, HRFM exhibits a smaller standard deviation in identified lead heights compared to ATL07, suggesting that HRFM achieves lower uncertainty by effectively filtering outliers in the lead detection process. It is noteworthy that during the summer melt season, the height range of lead segments expands for all methods due to the challenging surface-type classification.

Taken together, these differences in reference sea-level estimation might lead to the observed seasonal reversal in HRFM–ATL20 freeboard differences: HRFM freeboards are generally lower than ATL20 during winter, when ATL07 filtering removes many valid lead samples, but higher during summer, when melt-pond-affected ice is erroneously included in the

删除了: :
删除了: The d
删除了: reference
删除了: level
删除了: for freeboard estimation combining surface heights and surface-type classification.
删除了: Two examples from (a-d) 26 May 2019 and (e-h) 05 August 2019.…
删除了: images
删除了: HRFM
删除了: and
删除了: (c and g)
删除了: (d and h)
删除了: obtain the reference sea levels
删除了: -
删除了: reference sea level
删除了: Fig. 12
设置了格式: 字体: 加粗
删除了: Fig. 12
设置了格式: 字体: 加粗
删除了: Fig. 8
设置了格式: 字体: 小五, 加粗
删除了: Fig. 12
设置了格式: 字体: 加粗
删除了: Fig. 12
设置了格式: 字体: 加粗
设置了格式: 字体: 加粗
删除了: Fig. 12
删除了: Fig. 13
设置了格式: 字体: 小五, 加粗
删除了: Fig. 13
设置了格式: 字体: 小五, 加粗

reference sea-surface estimate. Similar winter–summer contrasts have been reported by Koo et al. (2023) in Antarctic sea ice freeboard, and are also consistent with recent findings by Petty et al. (2025), who showed that IS-2–derived sea ice thickness tends to be higher than CryoSat-2 estimates, with lower winter freeboards yielding improved inter-sensor consistency.

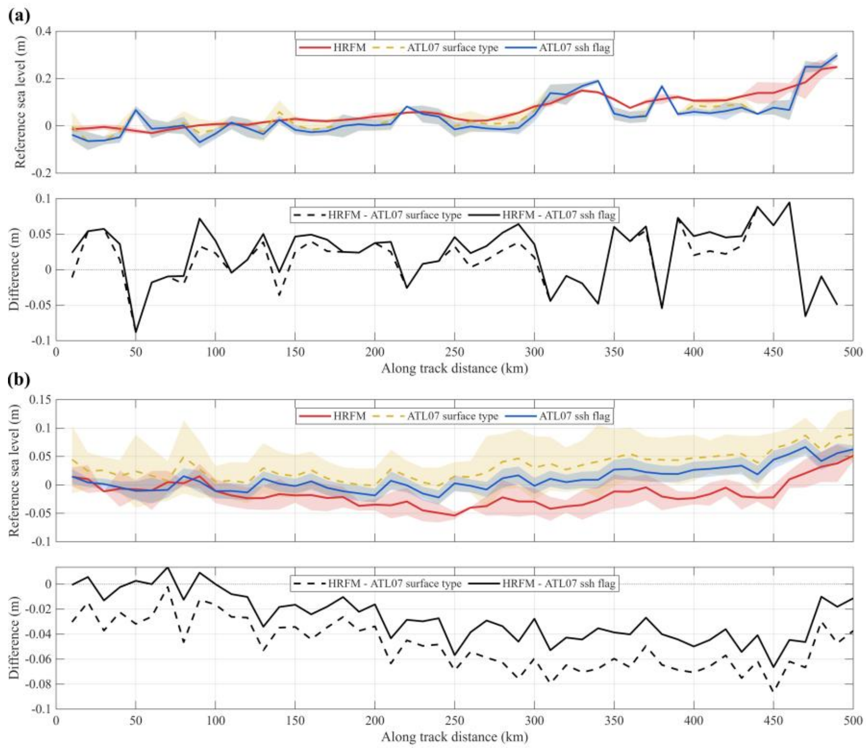

Figure 13. Determination of local sea-surface references along fifty consecutive10-km segments for ICESat-2 ground tracks acquired on (a) 26 May 2019 and (b) 5 August 2019. The upper panels show the local sea-surface references derived from HRFM (red solid line), ATL07 *surface_type* (yellow dashed line), and ATL07 *ssh_flag* (blue solid line), with shaded envelopes indicating ±1 standard deviation of the selected lead or sea-surface heights within each 10 km segment. The lower panels present the corresponding differences between HRFM and the two ATL07-based reference estimates.

删除了: :

删除了: reference sea levels

删除了: 0

删除了: reference sea levels

删除了: reference sea levels.

5.3 Possible limitations and future work

Despite the improved performance of HRFM in along-track surface-height retrieval, surface-type classification, and inter-beam consistency, several limitations remain and should be considered when interpreting the results of this study.

First, independent validation of gridded freeboard estimates at basin scale remains limited. Comparisons with ATM profiles provide useful validation of surface-height retrieval over thick, consolidated ice, but comparable independent observations are scarce for summer conditions and for large spatial scales (Saylam et al., 2025). Consequently, the absolute accuracy of gridded HRFM freeboards cannot yet be conclusively quantified. Future efforts combining airborne campaigns, autonomous platforms, and coordinated satellite observations will be essential for evaluating grid-scale freeboard products, particularly during the melt season.

Second, HRFM relies on a supervised machine-learning classifier trained using coincident optical imagery. While the leave-one-group-out cross-validation results indicate good performance across the tested beam types, surface conditions, and seasons, generalization to a broader range of atmospheric and illumination conditions remains an important consideration. Background photon rates are strongly affected by solar illumination and can become very low under low solar-elevation conditions. Under such conditions, classification uncertainty may increase because one of the key discriminative features becomes less informative. Following established ATL07 practices (Kwok et al., 2016, 2023), the background rate was excluded as a classification feature when the solar elevation angle was below 15°. Future work could address this limitation by incorporating a larger and more diverse training dataset and by exploring classification models that exploit along-track contextual information from multiple adjacent segments, rather than relying solely on features derived from individual signal segments. Such approaches may help reconcile robustness under low background conditions with improved separability of surface types, thereby further strengthening year-round surface-type classification and freeboard retrieval.

Third, although HRFM includes photon-density filtering, local height-window constraints, and after-pulse treatment, challenging atmospheric or pointing-related conditions can still affect photon retrieval and surface-type classification. In particular, cloud-attenuated returns, low signal strength, and potential pointing issues may reduce the reliability of individual segments. Future HRFM dataset construction will therefore benefit from incorporating additional ATL03 quality-control information, such as PODPPD-related flags and beam-angle information, to identify and flag potentially affected observations more systematically.

6 Conclusion

In this study, we developed and implemented the High-Resolution Freeboard Method (HRFM), a novel processing framework designed to retrieve high-resolution sea-ice freeboard directly from ICESat-2 ATL03 photon data. By improving signal photon extraction, surface-height retrieval, and surface-type classification, HRFM addresses several challenges in photon-counting laser altimetry over sea ice, including signal denoising in complex environments, detector after-pulse contamination, weak-beam underutilization, and melt-pond-related classification ambiguity.

HRFM employs a two-stage denoising strategy to extract signal photons associated with fine-scale ice morphology, including ridges, leads, and melt ponds, allowing along-track surface heights to be resolved at 5-m intervals. Validation against airborne ATM data demonstrates that HRFM achieves lower RMSE and higher correlation than ATL07 under the same non-

删除了: While comparisons with ATM profiles provide robust validation over thick, consolidated ice, comparable independent observations are scarce for summer conditions and for large spatial scales

删除了: the

删除了: demonstrate

删除了: stable

删除了: Background photon rates are strongly correlated with solar elevation and can vary by orders of magnitude under low solar angles.

删除了: Although surface-type classification could get noisier, Background rate was excluded as a classification feature when the solar elevation angle is below 15°, following established practices

删除了: optimize ICESat-2 ATL03 data for year-round, high-resolution sea ice monitoring.

删除了: long-standing

删除了: melt-pond interference

删除了: a

删除了: (0.08±0.01 m)

删除了: (r=0.95)

删除了: the

删除了:

shifted collocation framework. For the strong beam, HRFM reduces the RMSE from 0.12 ± 0.03 m for ATL07 to 0.08 ± 0.01 m and increases the correlation from 0.90 ± 0.05 to 0.95 ± 0.01. HRFM also better preserves small-scale ridge-related height variations and reduces lead-height fluctuations associated with lower-elevation after-pulse-contaminated photons.

Melt ponds remain a major obstacle for year-round freeboard retrieval as they reduce the contrast between sea ice and open-water leads. HRFM addresses this issue using a machine-learning surface-type classifier trained with 25 coincident Sentinel-2/ICESat-2 scenes, comprising more than two million labeled 5 m segments. The three-class classifier distinguishes sea ice, thin ice, and leads, while the final freeboard retrieval uses a conservative binary classifier in which thin ice is merged into the sea-ice class. This design reduces the risk of using uncertain thin-ice or melt-pond-affected segments as lead segments for local sea-surface reference construction. In the independent LOGO evaluation, the binary classifier achieves an overall accuracy of 0.99 for both strong and weak beams, supporting robust lead detection for freeboard retrieval.

Comparative analysis with the ATL20 product shows that while HRFM freeboard maps maintain consistent large-scale spatial patterns, they exhibit monthly mean differences of up to ±0.04 m. HRFM yields lower freeboard estimates in winter by retaining more valid lead samples and removing after-pulse photons, but produces higher freeboard estimates in summer by effectively excluding misclassified melt ponds in the determination of reference sea level.

An additional contribution of HRFM is the enhanced performance of weak beams, which yield freeboard estimates statistically consistent with those from strong beams. This capability might enable the joint utilization of all six ICESat-2 beams, increasing the actual area of sensed sea ice and reducing uncertainties in gridded freeboard products. Our ongoing work aims to extend HRFM to long-term ICESat-2 observations to construct continuous, cross-season records of sea ice freeboard and thickness, providing a high-fidelity dataset for sea ice forecasting and climate change investigations in the Arctic.

Appendix

Table A1 Summary of the 25 Sentinel-2/ICESat-2 coincident scenes used for training and validation.

No.	ICESat-2	Sentinel-2	Acquisition date	Time offsets (minutes)
1.	ATL03_20190712224936_02270404_006_02	S2_20190712T222111_20190712T222106_T13XDL	2019-07-12	28
2.	ATL03_20190805215948_05930404_006_02	S2_20190805T220101_20190805T220056_T11XMK	2019-08-05	01
3.	ATL03_20190622105707_13010304_006_02	S2_20190622T103631_20190622T103627_T44XMQ	2019-06-22	20
4.	ATL03_20200428205330_05090703_006_01	20200428T210019_20200428T210017_T09XVC	2020-04-28	07

删除了: product

删除了: , while better preserving small-scale surface variability. Notably, HRFM successfully minimizes height fluctuations over specular leads typically caused by detector saturation.

删除了: forming on sea ice surfaces during summer

删除了: are

删除了: to robust year-round freeboard retrieval,

删除了: they weaken classification contrast and challenge conventional threshold-based schemes

删除了: -based

删除了: optical images,

删除了: approximately two million ICESat-2 segments across all seasons

删除了: HRFM successfully separates true open-water leads from sea ice and melt ponds in summer and identifies thin gray ice as a distinct class in winter. This refined classification (overall accuracy > 0.98) ensures a more stable and consistent reference sea level.

删除了: seasonal

带格式的: 题注

带格式的: 居中

格式化表格

带格式的: 居中

带格式的: 居中

带格式的: 居中

带格式的: 居中

5.	ATL03_20200409210928_02190703_007_01	20200409T212031_20200409T212034_T10XDM	2020-04-09	11
6.	ATL03_20200327220004_00210703_006_01	S2_20200327T220119_20200327T220223_T09XWH	2020-03-27	01
7.	ATL03_20200410204349_02340703_006_02	S2_20200410T205021_20200410T205019_T11XMG	2020-04-10	06
8.	ATL03_20200314145921_12050603_006_01	S2_20200314T150909_20200314T150906_T28XEN	2020-03-14	09
9.	ATL03_20200322082530_13230603_006_01	S2_20200322T083621_20200322T083621_T43XEJ	2020-03-22	10
10.	ATL03_20210704231644_01731204_006_01	S2_20210704T232129_20210704T232125_T10XEQ	2021-07-04	04
11.	ATL03_20210714155137_03211204_006_01	S2_20210714T154911_20210714T154908_T28XDP	2021-07-14	02
12.	ATL03_20210711140000_02741204_006_01	S2_20210711T135731_20210711T135734_T31XFL	2021-07-11	02
13.	ATL03_20210624163315_00161204_006_01	S2_20210624T163839_20210624T163900_T28XES	2021-06-24	05
14.	ATL03_20220416233410_03801504_006_02	S2_20220416T234129_20220416T234130_T09XWM	2022-04-16	07
15.	ATL03_20220510145813_07411505_006_01	S2_20220510T145749_20220510T145752_T28XDM	2022-05-10	00
16.	ATL03_20220402135041_01601504_006_02	S2_20220402T135729_20220402T135727_T35XNL	2022-04-02	06
17.	ATL03_20220521101556_09061505_006_01	S2_20220521T101601_20220521T101603_T39XVJ	2022-05-21	00
18.	ATL03_20220423155204_04821504_006_02	S2_20220423T155831_20220423T155825_T28XES	2022-04-23	06
19.	ATL03_20220414225057_03491504_006_02	S2_20220414T230119_20220414T230114_T12XVR	2022-04-14	10
20.	ATL03_20220424231746_05021504_006_02	S2_20220424T230109_20220424T230111_T10XDR	2022-04-24	16

带格式的: 居中
带格式的: 居中
带格式的: 居中
带格式的: 居中
带格式的: 居中
带格式的: 居中
带格式的: 居中
带格式的: 居中
带格式的: 居中
带格式的: 居中
带格式的: 居中
带格式的: 居中
带格式的: 居中
带格式的: 居中
带格式的: 居中
带格式的: 居中

21.	ATL03_20220424135203_04961504_006_02	S2_20220424T134731_20220424T134731_T33XWL	2022-04-24	04
22.	ATL03_20230821234625_09592004_006_01	S2_20230822T002159_20230822T002154_T11XML	2023-08-22	30
23.	ATL03_20230821093750_09502004_006_02	S2_20230821T100601_20230821T100600_T45XWM	2023-08-21	28
24.	ATL03_20230827145527_10452004_006_02	S2_20230827T152811_20230827T152812_T31XEM	2023-08-27	30
25.	ATL03_20230831162132_11072004_006_02	S2_20230831T164851_20230831T164845_T27XWM	2023-08-31	27

Table A2 Summary of key algorithm parameters used for HRFM photon denoising, surface-height retrieval, surface-type classification, and freeboard estimation.

Parameters	Value
Coarse denoising along-track segment length	3 km
KDE horizontal scaling parameter,	25 / 100（strong beam / weak beam）
Local height-window constraint in coarse filtering	−2 m to +6 m relative to the modal height
Refined denoising local window length	10 m
Saturation threshold based on signal photon rate	16 / 4 photons per pulse（strong beam / weak beam）
Height histogram bin size for saturated windows	0.1 m
After-pulse removal threshold	Photons more than 0.3 m below the primary height peak
Density threshold for non-saturated refined denoising	10th percentile of coarse signal-photon densities within the local window
Surface-height retrieval resulotion	5 m
Background-rate normalization	Normalized to solar elevation angle of 20°
Number of GMM clusters for training-label generation	20 clusters
Number of RF decision trees	200
Maximum RF tree depth	20
Local sea-surface-reference window for freeboard retrieval	10 km
Outlier removal for lead elevations in each sea-level-reference window	3σ

Table A3 Summary of correction terms and mean sea-surface models used in HRFM and ATL07.

Correction term or reference model	HRFM	ATL07
Solid earth tide	inherited from ATL03	inherited from ATL03
Solid Earth pole tides	inherited from ATL03	inherited from ATL03
Ocean pole tides	inherited from ATL03	inherited from ATL03
Ocean loading	inherited from ATL03	inherited from ATL03
Total column atmospheric delay	inherited from ATL03	inherited from ATL03
Ocean tides	inherited from ATL03	inherited from ATL03
Long period equilibrium tides	inherited from ATL03	inherited from ATL03
Dynamic Atmospheric Correction	inherited from ATL03	inherited from ATL03
Mean sea surface	DTU 21	DTU 13/CS-2 merged product

2095 **Table A4 Confusion matrices and classification accuracy statistics for the HRFM surface-type classifier based on leave-one-group-out (LOGO) cross-validation, when thin-ice type is merged into sea-ice type**

Strong beam		Ground truth from Sentinel-2			Precision
		Sea ice	Lead	All	
HRFM surface type	Sea ice	930768	5315	936083	0.99
	Lead	3391	89815	93206	0.96
	All	934159	95130	1029289	
Recall		0.99	0.95		0.99

Weak beam		Ground truth from Sentinel-2			Precision
		Sea ice	Lead	All	
HRFM surface type	Sea ice	933895	8044	941939	0.99
	Lead	4448	77508	81956	0.95
	All	938343	85552	1023895	
Recall		0.99	0.91		0.99

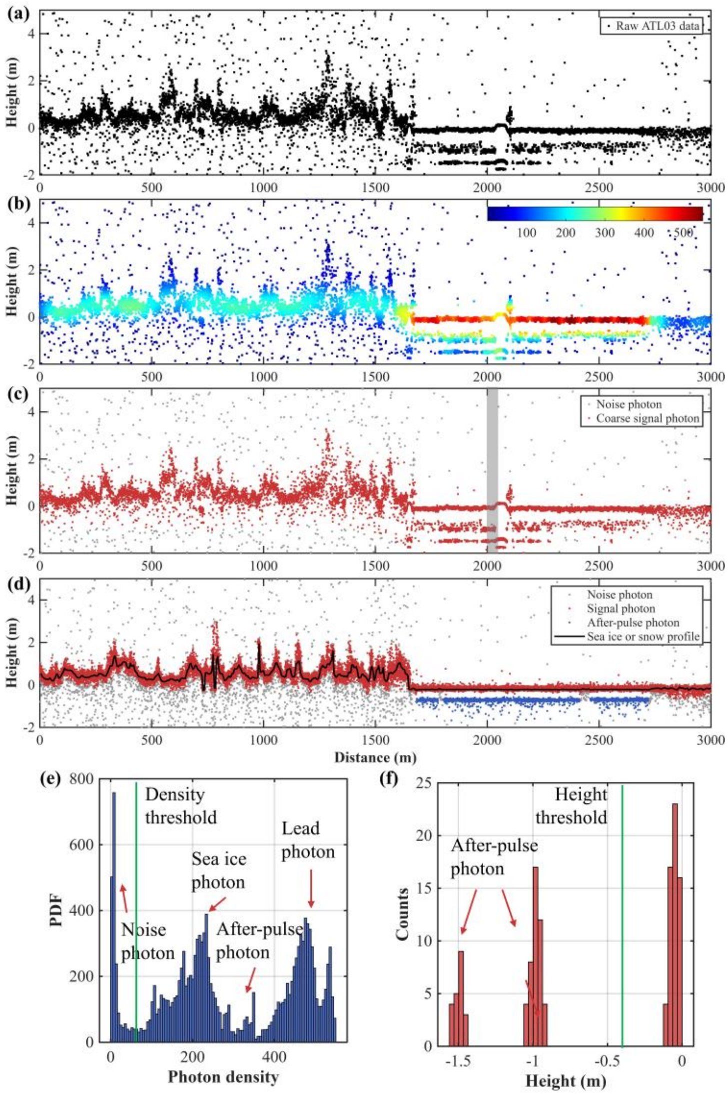

Figure A1. Same as Figure 3, but for the weak beam of ATL03_20190526002946_08820304_006_02 over the Lincoln Sea.

设置了格式: 字体: (中文) +中文正文 (宋体), (中文) 简体中文(中国大陆), (其他) 英语(美国)

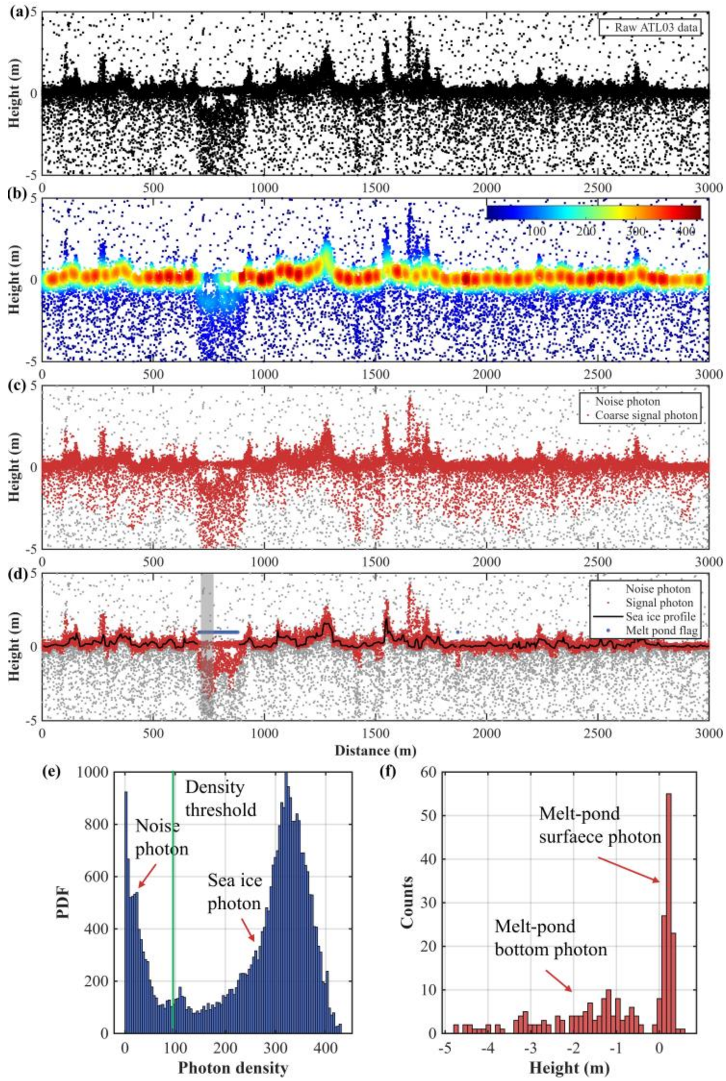

Figure A2. Same as in Figure 3, but for a melt pond example.

设置了格式: 字体: (中文) +中文正文 (宋体), (中文) 简体中文(中国大陆), (其他) 英语(美国)

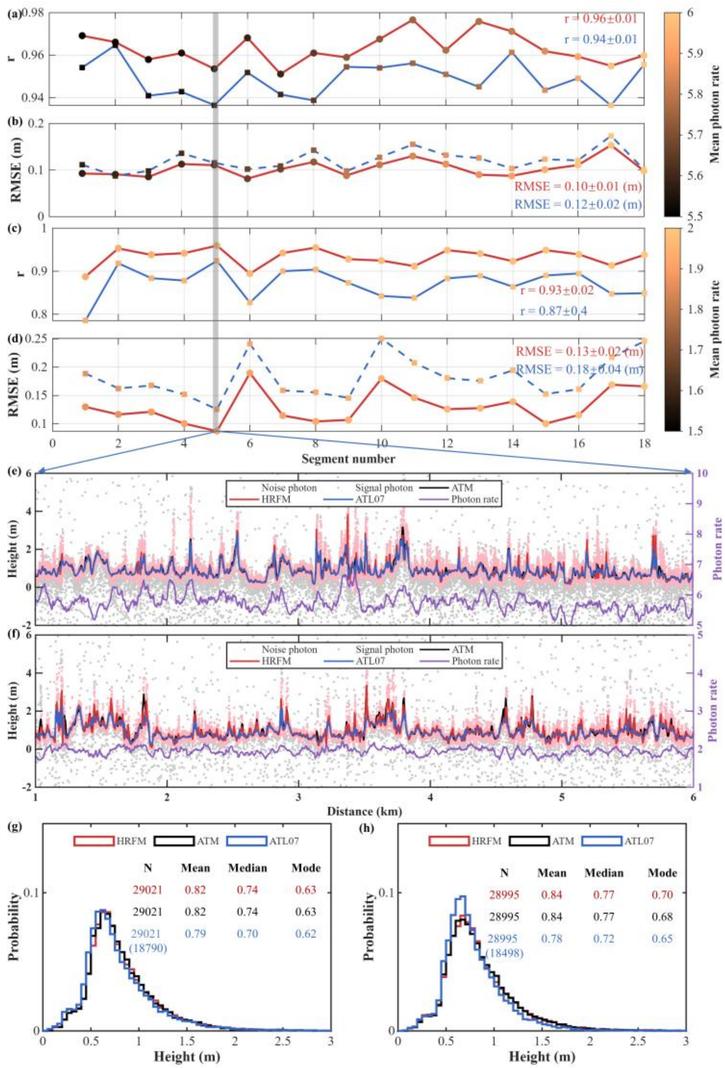

Figure A3. Same as in Figure 7, but for ATM observations acquired on 8 April 2019. The statistics are computed from 18 along-track segments.

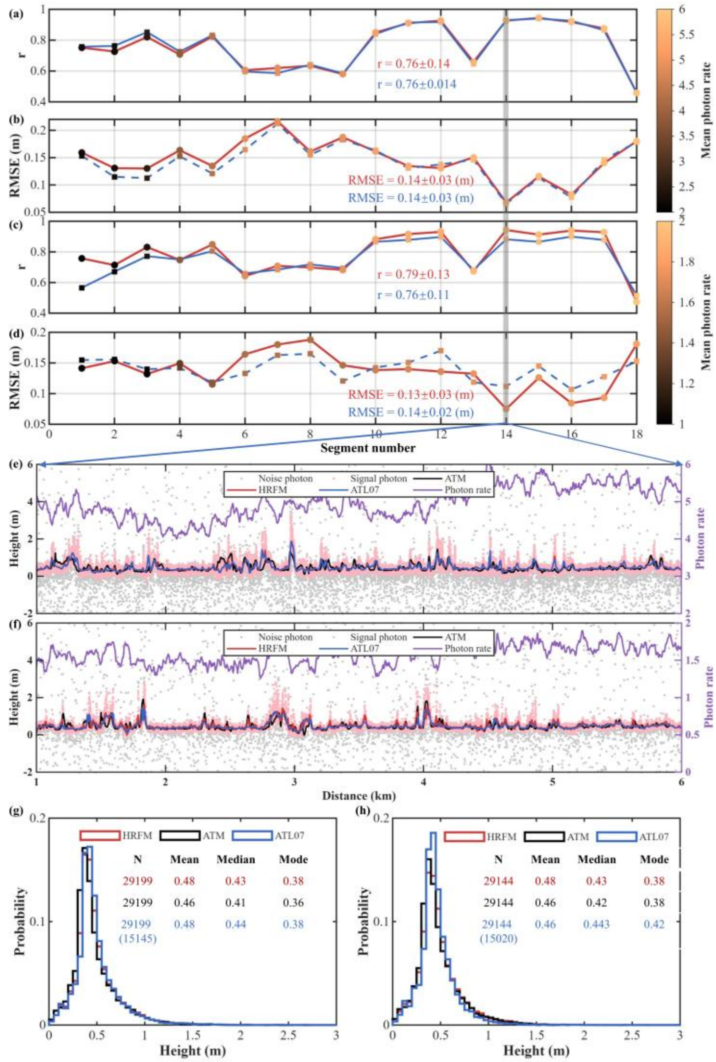

Figure A4. Same as in Figure 7, but for ATM observations acquired on 12 April 2019. The statistics are computed from 18 along-track segments.

带格式的: 居中

设置了格式: 英语(英国)

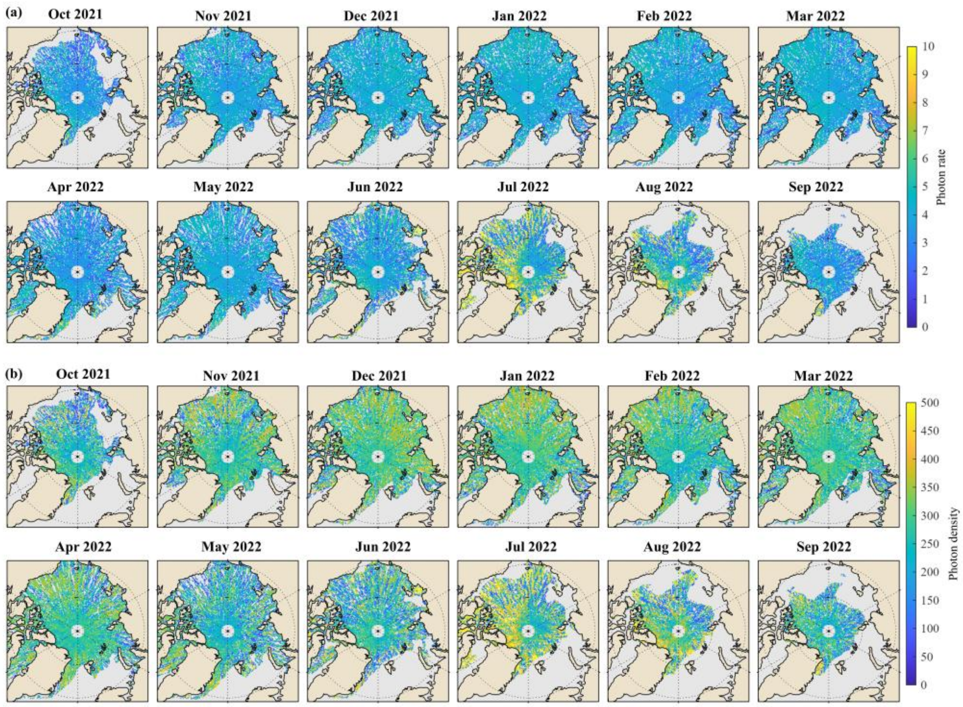

Figure A5. Monthly distributions of HRFM classification features from October 2021 to September 2022. (a) Monthly mean photon rate and (b) monthly mean photon density on the 25 km Arctic grid.

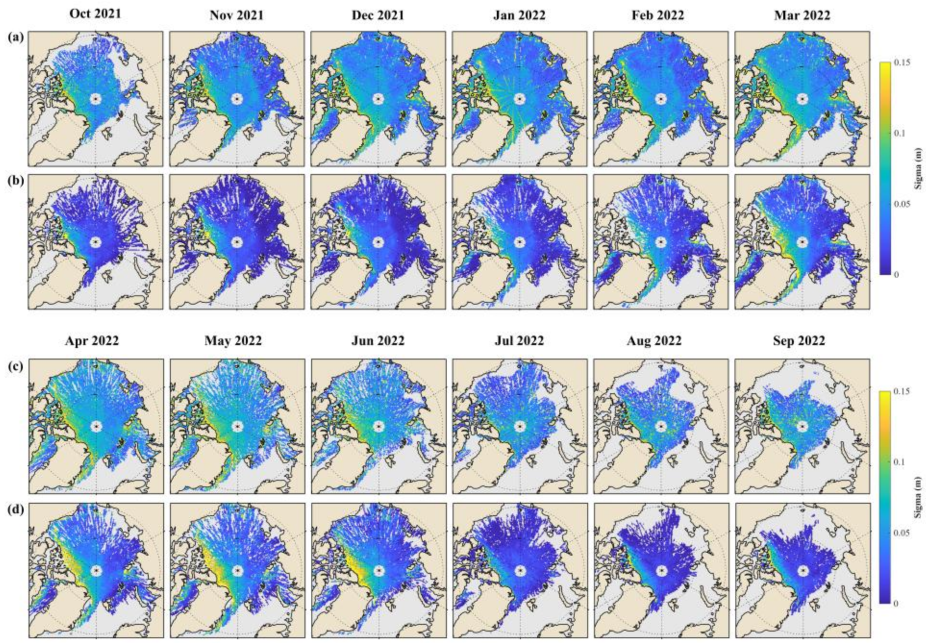

Figure A6. Monthly standard deviation of sea-ice freeboard within each 25 km grid cell from October 2021 to September 2022 for (a, c) HRFM and (b, d) ATL20.

带格式的: 正文

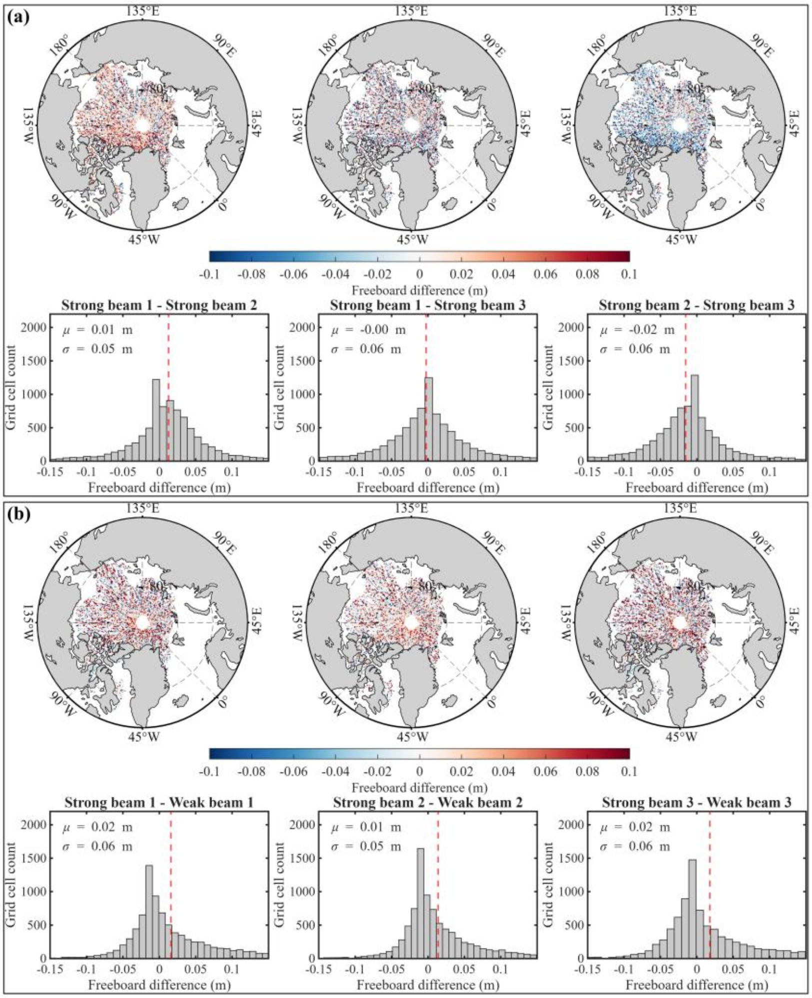

Figure A7. Same as in Figure 11, but for July 2022.

带格式的: 缩进: 首行缩进: 0 字符

Authorship contribution

Wenxuan Liu: Conceptualization, Data curation, Methodology, Validation, Writing – original draft, Visualization.
Ruibo Lei: Supervision, Writing – review & editing, Funding acquisition
Taoyong Jin: Supervision, Writing – review & editing,
Heyang Sun: Data curation, Writing – review & editing,
Michel Tsamados: Writing – review & editing.
Isolde A. Glissenaar: Data curation, Writing – review & editing.
Jack C. Landy: Writing – review & editing.
Yi Zhou: Writing – review & editing.

Data availability statement

The ICESat-2 ATL03 geolocated photon data, ATL07 sea-ice height and surface-type data, ATL20 gridded freeboard data, Airborne Topographic Mapper (ATM) data, and sea-ice concentration data are available from the National Snow and Ice Data Center: ATL03 Version 6 (https://nsidc.org/data/atl03/versions/6), ATL07 Version 6 (https://nsidc.org/data/atl07/versions/6), ATL20 Version 5 (https://nsidc.org/data/atl20/versions/5), ILATM1B (https://nsidc.org/data/ilatm1b), and the NOAA/NSIDC Climate Data Record of Passive Microwave Sea Ice Concentration Version 6 (https://nsidc.org/data/g02202/versions/6). The Sentinel-2 imagery was accessed through Google Earth Engine using the Sentinel-2 data collection (https://developers.google.com/earth-engine/datasets/catalog/sentinel-2). The processed along-track data described in this study are available at https://doi.org/10.5281/zenodo.21134059. The monthly gridded HRFM sea-ice freeboard generated in this study is available from Zenodo at https://doi.org/10.5281/zenodo.18452459.

删除了: The ICESat-2 ATL03 (geolocated photon), ATL07 (sea ice height and type), ATL20 (gridded freeboard), ATM, and sea ice concentration data are available through the National Snow and Ice Data Center (https://nsidc.org/data/atl03/versions/6, https://nsidc.org/data/atl07/versions/6, https://nsidc.org/data/atl20/versions/5), https://nsidc.org/data/ilatm1b, and https://nsidc.org/data/g02202/versions/6, respectively). The Sentinel-2 imagery was derived from Google Earth Engine at https://developers.google.com/earth-engine/datasets/catalog/sentinel-2. The HRFM-derived monthly sea ice freeboard can be accessed from Zenodo at https://doi.org/10.5281/zenodo.18452459.

Declaration of Competing Interest

At least one of the (co-)authors is a member of the editorial board of *The Cryosphere*.

Acknowledgements

The authors would like to thank the National Snow and Ice Data Center (NSIDC) for providing the ICESat-2 data and European Space Agency (ESA) for providing the Sentinel-2 data. WL and RL were supported by the National Natural Science Foundation of China under Grants 42530407, 42325604, and W2541018. MT would like to acknowledge support from the ESA Polar+ Snow Depth on Sea Ice Project (grant no. AO/1-10061/19/I-EF) and the CRISTAL LEVel-2 procEssor prototype and R&D Sea Ice and Iceberg (CLEV2ER) project (grant no. AO/111448/22/I-AG). IG and JL were supported by the European Research Council grant Summer Sea Ice in 3D (SI/3D) under #101077496.

References

Andersen, O. B., Rose, S. K., Abulaitijiang, A., Zhang, S., and Fleury, S.: The DTU21 global mean sea surface and first evaluation, Earth Syst. Sci. Data, 15, 4065–4075, https://doi.org/10.5194/essd-15-4065-2023, 2023.

Aylmer, J. R., Ferreira, D., and Feltham, D. L.: Impact of ocean heat transport on sea ice captured by a simple energy balance model, Commun Earth Environ, 5, 406, https://doi.org/10.1038/s43247-024-01565-7, 2024.

Bagnardi, M., Kurtz, N. T., Petty, A. A., and Kwok, R.: Sea Surface Height Anomalies of the Arctic Ocean From ICESat-2: A First Examination and Comparisons With CryoSat-2, Geophysical Research Letters, 48, e2021GL093155, https://doi.org/10.1029/2021GL093155, 2021.

Bateson, A. W., Feltham, D. L., Schröder, D., Hosekova, L., Ridley, J. K., and Aksenov, Y.: Impact of sea ice floe size distribution on seasonal fragmentation and melt of Arctic sea ice, The Cryosphere, 14, 403–428, https://doi.org/10.5194/tc-14-403-2020, 2020.

Breiman, L.: Random Forests, Machine Learning, 45, 5–32, https://doi.org/10.1023/A:1010933404324, 2001.

Brunt, K. M., Smith, B. E., Sutterley, T. C., Kurtz, N. T., and Neumann, T. A.: Comparisons of Satellite and Airborne Altimetry With Ground-Based Data From the Interior of the Antarctic Ice Sheet, Geophysical Research Letters, 48, e2020GL090572, https://doi.org/10.1029/2020GL090572, 2021.

Buckley, E. M., Farrell, S. L., Herzfeld, U. C., Webster, M. A., Trantow, T., Baney, O. N., Duncan, K. A., Han, H., and Lawson, M.: Observing the evolution of summer melt on multiyear sea ice with ICESat-2 and Sentinel-2, The Cryosphere, 17, 3695–3719, https://doi.org/10.5194/tc-17-3695-2023, 2023.

Buckley, E. M., Horvat, C., and Yoosiri, P.: Sea ice concentration estimates from ICESat-2 linear ice fraction – Part 1: Multi-sensor comparison of sea ice concentration products, The Cryosphere, 19, 4805–4818, https://doi.org/10.5194/tc-19-4805-2025, 2025.

Chu, C.-Y., Henderson, D. J., and Parmeter, C. F.: On discrete Epanechnikov kernel functions, Computational Statistics & Data Analysis, 116, 79–105, https://doi.org/10.1016/j.csda.2017.07.003, 2017.

Dandabathula, G., Roy, S., Ghatage, O., Bera, A. K., and Srivastav, S. K.: Determination of dust storm height using weak beam photons from ICESat-2 and relating with vertical wind profile, Atmospheric Environment, 354, 121276, https://doi.org/10.1016/j.atmosenv.2025.121276, 2025.

Dawson, G., Landy, J., Tsamados, M., Komarov, A. S., Howell, S., Heorton, H., and Krumpen, T.: A 10-year record of Arctic summer sea ice freeboard from CryoSat-2, Remote Sensing of Environment, 268, 112744, https://doi.org/10.1016/j.rse.2021.112744, 2022.

Duncan, K. and Farrell, S. L.: Determining Variability in Arctic Sea Ice Pressure Ridge Topography With ICESat-2, Geophysical Research Letters, 49, e2022GL100272, https://doi.org/10.1029/2022GL100272, 2022.

Farrell, S. L., Duncan, K., Buckley, E. M., Richter-Menge, J., and Li, R.: Mapping Sea Ice Surface Topography in High Fidelity With ICESat-2, Geophysical Research Letters, 47, e2020GL090708, https://doi.org/10.1029/2020GL090708, 2020.

Fredensborg Hansen, R. M., Rinne, E., and Skourup, H.: Classification of Sea Ice Types in the Arctic by Radar Echoes from SARAL/AltiKa, Remote Sensing, 13, 3183, https://doi.org/10.3390/rs13163183, 2021.

Herzfeld, U. C., Trantow, T. M., Han, H., Buckley, E., Farrell, S. L., and Lawson, M.: Automated Detection and Depth Determination of Melt Ponds on Sea Ice in ICESat-2 ATLAS Data—The Density-Dimension Algorithm for Bifurcating Sea-Ice Reflectors (DDA-Bifurcate-Seaice), IEEE Trans. Geosci. Remote Sensing, 61, 1–22, https://doi.org/10.1109/TGRS.2023.3268073, 2023.

Kacimi, S. and Kwok, R.: Arctic Snow Depth, Ice Thickness, and Volume From ICESat-2 and CryoSat-2: 2018–2021, Geophysical Research Letters, 49, e2021GL097448, https://doi.org/10.1029/2021GL097448, 2022.

Kacimi, S. and Kwok, R.: Two Decades of Arctic Sea-Ice Thickness from Satellite Altimeters: Retrieval Approaches and Record of Changes (2003–2023), Remote Sensing, 16, 2983, https://doi.org/10.3390/rs16162983, 2024.

Koo, Y., Xie, H., Kurtz, N. T., Ackley, S. F., and Wang, W.: Sea ice surface type classification of ICESat-2 ATL07 data by using data-driven machine learning model: Ross Sea, Antarctic as an example, Remote Sensing of Environment, 296, 113726, https://doi.org/10.1016/j.rse.2023.113726, 2023.

Koo, Y., Xie, H., Meier, W. N., Ackley, S. F., and Kurtz, N. T.: Detection of multi-year ex-fast ice in the Weddell Sea, Antarctica, using ICESat-2 satellite altimeter data, Remote Sensing of Environment, 325, 114750, https://doi.org/10.1016/j.rse.2025.114750, 2025.

Kortum, K., Singha, S., and Spreen, G.: Sea ice freeboard extrapolation from ICESat-2 to Sentinel-1, The Cryosphere, 19, 4701–4714, https://doi.org/10.5194/tc-19-4701-2025, 2025.

Krabill, W. B., Abdalati, W., Frederick, E. B., Manizade, S. S., Martin, C. F., Sonntag, J. G., Swift, R. N., Thomas, R. H., and Yungel, J. G.: Aircraft laser altimetry measurement of elevation changes of the greenland ice sheet: technique and accuracy assessment, Journal of Geodynamics, 34, 357–376, https://doi.org/10.1016/S0264-3707(02)00040-6, 2002.

Krumpen, T., Von Albedyll, L., Bünger, H. J., Castellani, G., Hartmann, J., Helm, V., Hendricks, S., Hutter, N., Landy, J. C., Lisovski, S., Lüpkes, C., Rohde, J., Suhrhoff, M., and Haas, C.: Smoother sea ice with fewer pressure ridges in a more dynamic Arctic, Nat. Clim. Chang., 15, 66–72, https://doi.org/10.1038/s41558-024-02199-5, 2025.

Kurtz, N. T. and Markus, T.: Satellite observations of Antarctic sea ice thickness and volume, J. Geophys. Res., 117, 2012JC008141, https://doi.org/10.1029/2012JC008141, 2012.

Kwok, R., Cunningham, G. F., Hoffmann, J., and Markus, T.: Testing the ice-water discrimination and freeboard retrieval algorithms for the ICESat-2 mission, Remote Sensing of Environment, 183, 13–25, https://doi.org/10.1016/j.rse.2016.05.011, 2016.

Kwok, R., Kacimi, S., Markus, T., Kurtz, N. T., Studinger, M., Sonntag, J. G., Manizade, S. S., Boisvert, L. N., and Harbeck, J. P.: ICESat-2 Surface Height and Sea Ice Freeboard Assessed With ATM Lidar Acquisitions From Operation IceBridge, Geophysical Research Letters, 46, 11228–11236, https://doi.org/10.1029/2019GL084976, 2019a.

Kwok, R., Markus, T., Kurtz, N. T., Petty, A. A., Neumann, T. A., Farrell, S. L., Cunningham, G. F., Hancock, D. W., Ivanoff, A., and Wimert, J. T.: Surface Height and Sea Ice Freeboard of the Arctic Ocean From ICESat-2: Characteristics and Early Results, JGR Oceans, 124, 6942–6959, https://doi.org/10.1029/2019JC015486, 2019b.

Kwok, R., Petty, A. A., Bagnardi, M., Kurtz, N. T., Cunningham, G. F., Ivanoff, A., and Kacimi, S.: Refining the sea surface identification approach for determining freeboards in the ICESat-2 sea ice products, The Cryosphere, 15, 821–833, https://doi.org/10.5194/tc-15-821-2021, 2021.

Kwok, R., A. A. Petty, G. Cunningham, T. Markus, D. Hancock, A. Ivanoff, J. Wimert, M. Bagnardi, N. Kurtz, and Team, T. Ices.-2 S.: ATLAS/ICESat-2 L3A Sea Ice Height, Version 6, https://doi.org/10.5067/ATLAS/ATL07.006, 2023.

Kwok, R., Kurtz, N., Wimert, J., Petty, A., Cunningham, G., Markus, T., Hancock, D., Ivanoff, A., Bagnardi, M., Herzfeld, U., Trantow, T., and ICESat-2 Science Team: Ice, Cloud, and Land Elevation Satellite (ICESat-2) Project Algorithm Theoretical Basis Document (ATBD) for Sea Ice Products, version 7, https://doi.org/10.5067/KPMXUOH7TNIY, 2026.

Landy, J. C., Dawson, G. J., Tsamados, M., Bushuk, M., Stroeve, J. C., Howell, S. E. L., Krumpen, T., Babb, D. G., Komarov, A. S., Heorton, H. D. B. S., Belter, H. J., and Aksenov, Y.: A year-round satellite sea-ice thickness record from CryoSat-2, Nature, 609, 517–522, https://doi.org/10.1038/s41586-022-05058-5, 2022.

Laxon, S. W., Giles, K. A., Ridout, A. L., Wingham, D. J., Willatt, R., Cullen, R., Kwok, R., Schweiger, A., Zhang, J., Haas, C., Hendricks, S., Krishfield, R., Kurtz, N., Farrell, S., and Davidson, M.: CryoSat-2 estimates of Arctic sea ice thickness and volume, Geophysical Research Letters, 40, 732–737, https://doi.org/10.1002/grl.50193, 2013.

Light, B., Smith, M. M., Perovich, D. K., Webster, M. A., Holland, M. M., Linhardt, F., Raphael, I. A., Clemens-Sewall, D., Macfarlane, A. R., Anhaus, P., and Bailey, D. A.: Arctic sea ice albedo: Spectral composition, spatial heterogeneity, and temporal evolution observed during the MOSAiC drift, Elementa: Science of the Anthropocene, 10, 000103, https://doi.org/10.1525/elementa.2021.000103, 2022.

Liu, A., Yang, J., Bao, Q., Vitart, F., Liu, J., Liang, X., Lu, M., Kim, S.-J., Gong, D., Tian, Z., and Liu, H.: Assimilating summer sea ice thickness enhances predictions of Arctic sea ice and surrounding atmosphere within two months, npj Clim Atmos Sci, 8, 210, https://doi.org/10.1038/s41612-025-01050-8, 2025a.

Liu, Q., Babanin, A. V., Zieger, S., Young, I. R., and Guan, C.: Wind and Wave Climate in the Arctic Ocean as Observed by Altimeters, Journal of Climate, 29, 7957–7975, https://doi.org/10.1175/JCLI-D-16-0219.1, 2016.

Liu, W., Tsamados, M., Petty, A., Jin, T., Chen, W., and Stroeve, J.: Enhanced sea ice classification for ICESat-2 using combined unsupervised and supervised machine learning, Remote Sensing of Environment, 318, 114607, https://doi.org/10.1016/j.rse.2025.114607, 2025b.

Lu, X., Hu, Y., Yang, Y., Vaughan, M., Palm, S., Trepte, C., Omar, A., Lucker, P., and Baize, R.: Enabling Value Added Scientific Applications of ICESat-2 Data With Effective Removal of Afterpulses, Earth and Space Science, 8, e2021EA001729, https://doi.org/10.1029/2021EA001729, 2021.

Lu, X., Hu, Y., Omar, A., and Trepte, C. R.: Bathymetry and Agricultural Crop Studies From ICESat-2: The Density-Dimension Algorithm, Earth and Space Science, 12, e2024EA004037, https://doi.org/10.1029/2024EA004037, 2025.

Lund, J., Sapp, L., Kubiczek, J. M., Böhm, A. M., and Von Bock Und Polach, F.: Simulated ice loads on a ship propeller and comparison with full-scale measurements, Marine Structures, 104, 103879, https://doi.org/10.1016/j.marstruc.2025.103879, 2025.

Macias-Fauria, M. and Post, E.: Effects of sea ice on Arctic biota: an emerging crisis discipline, Biol. Lett., 14, 20170702, https://doi.org/10.1098/rsbl.2017.0702, 2018.

Magruder, L., Brunt, K., and Alonzo, M.: Early ICESat-2 on-orbit Geolocation Validation Using Ground-Based Corner Cube Retro-Reflectors, Remote Sensing, 12, 3653, https://doi.org/10.3390/rs12213653, 2020.

Magruder, L. A., Neumann, T., Kurtz, N., Sutterley, T. C., Hancock, D., Vornberger, P., Robbins, J., and Smith, B.: Assessment of the Ice, Cloud, and Land Elevation Satellite-2 Performance Against Prime Mission Science Requirements, Earth and Space Science, 12, e2025EA004221, https://doi.org/10.1029/2025EA004221, 2025.

Markus, T., Neumann, T., Martino, A., Abdalati, W., Brunt, K., Csatho, B., Farrell, S., Fricker, H., Gardner, A., Harding, D., Jasinski, M., Kwok, R., Magruder, L., Lubin, D., Luthcke, S., Morison, J., Nelson, R., Neuenschwander, A., Palm, S., Popescu, S., Shum, C., Schutz, B. E., Smith, B., Yang, Y., and Zwally, J.: The Ice, Cloud, and land Elevation Satellite-2 (ICESat-2): Science requirements, concept, and implementation, Remote Sensing of Environment, 190, 260–273, https://doi.org/10.1016/j.rse.2016.12.029, 2017.

Mchedlishvili, A., Lüpkes, C., Petty, A., Tsamados, M., and Spreen, G.: New estimates of pan-Arctic sea ice–atmosphere neutral drag coefficients from ICESat-2 elevation data, The Cryosphere, 17, 4103–4131, https://doi.org/10.5194/tc-17-4103-2023, 2023.

McPhee, M.: Air-Ice-Ocean Interaction, Springer New York, New York, NY, https://doi.org/10.1007/978-0-387-78335-2, 2008.

Mugunthan, J. S., Duguay, C. R., and Zakharova, E.: Machine learning based classification of lake ice and open water from Sentinel-3 SAR altimetry waveforms, Remote Sensing of Environment, 299, 113891, https://doi.org/10.1016/j.rse.2023.113891, 2023.

Muilwijk, M., Hattermann, T., Martin, T., and Granskog, M. A.: Future sea ice weakening amplifies wind-driven trends in surface stress and Arctic Ocean spin-up, Nat Commun, 15, 6889, https://doi.org/10.1038/s41467-024-50874-0, 2024.

Neumann, T. A., Martino, A. J., Markus, T., Bae, S., Bock, M. R., Brenner, A. C., Brunt, K. M., Cavanaugh, J., Fernandes, S. T., Hancock, D. W., Harbeck, K., Lee, J., Kurtz, N. T., Luers, P. J., Luthcke, S. B., Magruder, L., Pennington, T. A., Ramos-Izquierdo, L., Rebold, T., Skoog, J., and Thomas, T. C.: The Ice, Cloud, and Land Elevation Satellite – 2 mission: A global geolocated photon product derived from the Advanced Topographic Laser Altimeter System, Remote Sensing of Environment, 233, 111325, https://doi.org/10.1016/j.rse.2019.111325, 2019.

Neumann, T. A., A. Brenner, D. Hancock, J. Robbins, J. Saba, K. Harbeck, A. Gibbons, J. Lee, S. B. Luthcke, and T. Rebold: ATLAS/ICESat-2 L2A Global Geolocated Photon Data, Version 6, https://doi.org/10.5067/ATLAS/ATL03.006, 2023.

Petty, A., Cabaj, A., and Landy, J.: Initial assessment of all-season Arctic sea ice thickness from ICESat-2, J. Glaciol., 1–39, https://doi.org/10.1017/jog.2025.10119, 2025.

Petty, A. A., Kurtz, N. T., Kwok, R., Markus, T., and Neumann, T. A.: Winter Arctic Sea Ice Thickness From ICESat-2 Freeboards, JGR Oceans, 125, e2019JC015764, https://doi.org/10.1029/2019JC015764, 2020.

Petty, A. A., Bagnardi, M., Kurtz, N. T., Tilling, R., Fons, S., Armitage, T., Horvat, C., and Kwok, R.: Assessment of ICESat-2 Sea Ice Surface Classification with Sentinel-2 Imagery: Implications for Freeboard and New Estimates of Lead and Floe Geometry, Earth and Space Science, 8, e2020EA001491, https://doi.org/10.1029/2020EA001491, 2021.

Petty, A. A., Keeney, N., Cabaj, A., Kushner, P., and Bagnardi, M.: Winter Arctic sea ice thickness from ICESat-2: upgrades to freeboard and snow loading estimates and an assessment of the first three winters of data collection, The Cryosphere, 17, 127–156, https://doi.org/10.5194/tc-17-127-2023, 2023.

Pratte, I., Braune, B. M., Hobson, K. A., and Mallory, M. L.: Variable sea-ice conditions influence trophic dynamics in an Arctic community of marine top predators, Ecology and Evolution, 9, 7639–7651, https://doi.org/10.1002/ece3.5313, 2019.

Quartly, G., Rinne, E., Passaro, M., Andersen, O., Dinardo, S., Fleury, S., Guillot, A., Hendricks, S., Kurekin, A., Müller, F., Ricker, R., Skourup, H., and Tsamados, M.: Retrieving Sea Level and Freeboard in the Arctic: A Review of Current Radar Altimetry Methodologies and Future Perspectives, Remote Sensing, 11, 881, https://doi.org/10.3390/rs11070881, 2019.

Ricker, R., Fons, S., Jutila, A., Hutter, N., Duncan, K., Farrell, S. L., Kurtz, N. T., and Fredensborg Hansen, R. M.: Linking scales of sea ice surface topography: evaluation of ICESat-2 measurements with coincident helicopter laser scanning during MOSAiC, The Cryosphere, 17, 1411–1429, https://doi.org/10.5194/tc-17-1411-2023, 2023.

Ridley, J. K., Blockley, E. W., and Ringer, M. A.: Arctic Sea Ice Causes Seasonal Differences in the Response of Arctic Water Vapor to Climate Warming in the CMIP6 Model, HadGEM3-GC3.1, Geophysical Research Letters, 50, e2022GL102541, https://doi.org/10.1029/2022GL102541, 2023.

Saylam, K., Averett, A. R., Andrews, J. R., Short, S. R., Kurtz, N. T., and Tilling, R. L.: Airborne Lidar to Verify ICESat-2 Arctic Summer Sea Ice Heights and Melt Pond Depths: Calibration and Validation Campaign, Greenland 2022, Earth and Space Science, 12, e2024EA004100, https://doi.org/10.1029/2024EA004100, 2025.

Schutz, B. E., Zwally, H. J., Shuman, C. A., Hancock, D., and DiMarzio, J. P.: Overview of the ICESat Mission, Geophysical Research Letters, 32, 2005GL024009, https://doi.org/10.1029/2005GL024009, 2005.

Shen, X., Zhang, J., Meng, J., Zhang, J., and Ke, C.: Sea ice type classification based on random forest machine learning with Cryosat-2 altimeter data, in: 2017 International Workshop on Remote Sensing with Intelligent Processing (RSIP), 2017 International Workshop on Remote Sensing with Intelligent Processing (RSIP), 1–5, https://doi.org/10.1109/RSIP.2017.7958792, 2017.

Shu, Y., Cui, H., Song, L., Gan, L., Xu, S., Wu, J., and Zheng, C.: Influence of sea ice on ship routes and speed along the Arctic Northeast Passage, Ocean & Coastal Management, 256, 107320, https://doi.org/10.1016/j.ocecoaman.2024.107320, 2024.

Song, R., Mu, L., Loza, S. N., Kauker, F., and Chen, X.: Assimilating Summer Sea-Ice Thickness Observations Improves Arctic Sea-Ice Forecast, Geophysical Research Letters, 51, e2024GL110405, https://doi.org/10.1029/2024GL110405, 2024.

Stroeve, J. and Notz, D.: Changing state of Arctic sea ice across all seasons, Environ. Res. Lett., 13, 103001, https://doi.org/10.1088/1748-9326/aade56, 2018.

Sun, L., Alexander, M., and Deser, C.: Evolution of the Global Coupled Climate Response to Arctic Sea Ice Loss during 1990–2090 and Its Contribution to Climate Change, J. Climate, 31, 7823–7843, https://doi.org/10.1175/JCLI-D-18-0134.1, 2018.

Tilling, R., Kurtz, N. T., Bagnardi, M., Petty, A. A., and Kwok, R.: Detection of Melt Ponds on Arctic Summer Sea Ice From ICESat-2, Geophysical Research Letters, 47, e2020GL090644, https://doi.org/10.1029/2020GL090644, 2020.

Timmermans, M. and Marshall, J.: Understanding Arctic Ocean Circulation: A Review of Ocean Dynamics in a Changing Climate, JGR Oceans, 125, e2018JC014378, https://doi.org/10.1029/2018JC014378, 2020.

Uhlíková, T., Vihma, T., Karpechko, A. Y., and Uotila, P.: Effects of Arctic sea-ice concentration on turbulent surface fluxes in four atmospheric reanalyses, The Cryosphere, 18, 957–976, https://doi.org/10.5194/tc-18-957-2024, 2024.

Von Schuckmann, K., Minière, A., Gues, F., Cuesta-Valero, F. J., Kirchengast, G., Adusumilli, S., Straneo, F., Ablain, M., Allan, R. P., Barker, P. M., Beltrami, H., Blazquez, A., Boyer, T., Cheng, L., Church, J., Desbruyeres, D., Dolman, H., Domingues, C. M., García-García, A., Giglio, D., Gilson, J. E., Gorfer, M., Haimberger, L., Hakuba, M. Z., Hendricks, S., Hosoda, S., Johnson, G. C., Killick, R., King, B., Kolodziejczyk, N., Korosov, A., Krinner, G., Kuusela, M., Landerer, F. W., Langer, M., Lavergne, T., Lawrence, I., Li, Y., Lyman, J., Marti, F., Marzeion, B., Mayer, M., MacDougall, A. H., McDougall, T., Monselesan, D. P., Nitzbon, J., Otosaka, I., Peng, J., Purkey, S., Roemmich, D., Sato, K., Sato, K., Savita, A., Schweiger, A., Shepherd, A., Seneviratne, S. I., Simons, L., Slater, D. A., Slater, T., Steiner, A. K., Suga, T., Szekely, T., Thiery, W., Timmermans, M.-L., Vanderkelen, I., Wjiffels, S. E., Wu, T., and Zemp, M.: Heat stored in the Earth system 1960–2020: where does the energy go?, Earth Syst. Sci. Data, 15, 1675–1709, https://doi.org/10.5194/essd-15-1675-2023, 2023.

Wang, C., Su, H., Zhai, C., Zheng, J., Yu, S., Mo, H., Wang, Y., and Jiang, L.: Recent slowing of Arctic sea ice melt tied to multidecadal NAO variability, Nat Commun, 16, 8504, https://doi.org/10.1038/s41467-025-63520-0, 2025.

Wimert, J., Kurtz, N., Buckley, E., Lee, J., Farrell, S., Duncan, K., and Robertson, K.: Improvements to ICESat-2 Sea Ice Data Products: Enhanced Resolution of Rough Terrain, in: IGARSS 2025 - 2025 IEEE International Geoscience and Remote Sensing Symposium, IGARSS 2025 - 2025 IEEE International Geoscience and Remote Sensing Symposium, 1736–1739, https://doi.org/10.1109/IGARSS55030.2025.11242262, 2025.

Wingham, D. J., Francis, C. R., Baker, S., Bouzinac, C., Brockley, D., Cullen, R., De Chateau-Thierry, P., Laxon, S. W., Mallow, U., Mavrocordatos, C., Phalippou, L., Ratier, G., Rey, L., Rostan, F., Viau, P., and Wallis, D. W.: CryoSat: A mission to determine the fluctuations in Earth's land and marine ice fields, Advances in Space Research, 37, 841–871, https://doi.org/10.1016/j.asr.2005.07.027, 2006.

Zhang, Z., Liu, X., Ma, Y., Xu, N., Zhang, W., and Li, S.: Signal Photon Extraction Method for Weak Beam Data of ICESat-2 Using Information Provided by Strong Beam Data in Mountainous Areas, Remote Sensing, 13, 863, https://doi.org/10.3390/rs13050863, 2021.

Zhou, C., Wang, Q., Tan, I., Zhang, L., Zelinka, M. D., Wang, M., and Bloch-Johnson, J.: Sea ice pattern effect on Earth's energy budget is characterized by hemispheric asymmetry, Sci. Adv., 11, eadr4248, https://doi.org/10.1126/sciadv.adr4248, 2025.

设置了格式: 字体: (中文) +中文正文 (宋体), (中文) 简体中文(中国大陆)

带格式的: 正文

删除了: Appendix A
Table A1 Confusion matrices and classification accuracy statistics for the HRFM surface-type classifier based on leave-one-group-out (LOGO) cross-validation, when thin-ice type is merged into sea-ice type
Strong beam

...